Viscosity Measurements at High Pressures: A Critical Appraisal of Corrections to Stokes' Law

Aaron Wolfgang Ashley, Mainak Mookherjee, Man Xu, Tony Yu, Geeth Manthilake, Yanbin Wang

JGR Solid Earth

RESEARCH ARTICLE
10.1029/2023JB028489

Viscosity Measurements at High Pressures: A Critical Appraisal of Corrections to Stokes' Law

Aaron Wolfgang Ashley[1], Mainak Mookherjee[1,2], Man Xu[3], Tony Yu[3], Geeth Manthilake[4], and Yanbin Wang[3]

[1]Earth Materials Laboratory, Department of Earth, Ocean and Atmospheric Sciences, Florida State University, Tallahassee, FL, USA, [2]Earth and Planets Laboratory, Carnegie Institute for Science, Washington, DC, USA, [3]Center for Advanced Radiation Sources, The University of Chicago, Chicago, IL, USA, [4]Laboratoire Magmas et Volcans CNRS, IRD, OPGC, Université Clermont Auvergne, Clermont-Ferrand, France

Key Points:

- We performed high-pressure experiments to evaluate drag acting on falling spheres in Stokes' Law viscometry
- We evaluated different correction schemes for Stokes' Law and used Monte Carlo simulations to evaluate the uncertainties in each scheme
- The best correction may be for drag due to the chamber walls, while other corrections may be ineffective or overcorrect the viscosity

Supporting Information:

Supporting Information may be found in the online version of this article.

Correspondence to:

A. W. Ashley,
awashley@fsu.edu

Citation:

Ashley, A. W., Mookherjee, M., Xu, M., Yu, T., Manthilake, G., & Wang, Y. (2024). Viscosity measurements at high pressures: A critical appraisal of corrections to Stokes' Law. *Journal of Geophysical Research: Solid Earth*, *129*, e2023JB028489. https://doi.org/10.1029/2023JB028489

Received 7 DEC 2023
Accepted 10 APR 2024

Author Contributions:

Conceptualization: Aaron Wolfgang Ashley, Mainak Mookherjee, Yanbin Wang
Formal analysis: Aaron Wolfgang Ashley
Funding acquisition: Aaron Wolfgang Ashley, Mainak Mookherjee, Yanbin Wang
Investigation: Aaron Wolfgang Ashley
Methodology: Aaron Wolfgang Ashley, Mainak Mookherjee, Man Xu, Tony Yu, Geeth Manthilake, Yanbin Wang
Project administration: Mainak Mookherjee, Yanbin Wang
Resources: Mainak Mookherjee, Geeth Manthilake, Yanbin Wang

Abstract Fluids and melts in planetary interiors significantly influence geodynamic processes from volcanism to global-scale differentiation. The roles of these geofluids depend on their viscosities (η). Constraining geofluid η at relevant pressures and temperatures relies on laboratory-based measurements and is most widely done using Stokes' Law viscometry with falling spheres. Yet small sample chambers required by high-pressure experiments introduce significant drag on the spheres. Several correction schemes are available for Stokes' Law but there is no consensus on the best scheme(s) for high-pressure experiments. We completed high-pressure experiments to test the effects of (a) the relative size of the sphere diameter to the chamber diameter and (b) the top and bottom of the chamber, that is, the ends, on the sphere velocities. We examined the influence of current correction schemes on the estimated viscosity using Monte Carlo simulations. We also compared previous viscometry work on various geofluids in different experimental setups/geometries. We find the common schemes for Stokes' Law produce statistically distinct values of η. When inertia of the sphere is negligible, the most appropriate scheme may be the Faxén correction for the chamber walls. Correction for drag due to the chamber ends depends on the precision in the sinking distance and may be ineffective with decreasing sphere size. Combining the wall and end corrections may overcorrect η. We also suggest the uncertainty in η is best captured by the correction rather than propagated errors from experimental parameters. We develop an overlying view of Stokes' Law viscometry at high pressures.

Plain Language Summary Liquids and vapors, collectively known as fluids, occur throughout the Earth and other planets. Compared to solid rock, fluids can move rapidly due to their lower viscosities and hence influence and promote important geologic processes. The large span of pressures and temperatures inside planets influences the viscosities of fluids. Measuring a fluid viscosity at relevant pressures is most often done by tracking a sphere that sinks in the fluid. The sinking speed of the sphere is converted to the fluid viscosity by balancing forces which cause and oppose the sinking, known as Stokes' Law. To create the right pressures, unique devices are used which require small chambers to house the fluid and sphere. The small chambers affect the sinking speeds and hence Stokes' Law becomes inaccurate. There are several corrections for the chamber effects on the sphere. However, there is no consensus on which correction should be used for high-pressure measurements. We examined the chamber effects on the sinking speeds in high-pressure experiments. We calculated the fluid viscosity using each correction and considered the uncertainties. We find that the corrections produce unique values of viscosity and are not equal. Future work should carefully consider the choice in correction.

1. Introduction

Volatile-rich fluids and molten silicates/metals often promote rapid geologic processes, such as volcanism, due to their high mobilities compared to solid rock. The viscosity (η) of these "geofluids" directly influences the rates at which they move in a host matrix and their specific roles in geologic processes. A classic example is the influence that the viscosity of silicate melts has on the volcanic eruption style of lavas. At the surface, lavas that are rich in silica, such as rhyolitic lavas with ≥69 wt% SiO_2, tend to erupt in explosive style due to their high viscosities ($\geq 10^5$ Pa s) (Castro & Dingwell, 2009; Dingwell, 1995). In contrast, silica-poor lavas, such as basalts with between 45 and 52 wt% silica (Dingwell, 1995), tend to display lower viscosities and flow upon eruption, that is, display an effusive eruption style.

Software: Aaron Wolfgang Ashley
Supervision: Mainak Mookherjee, Yanbin Wang
Validation: Aaron Wolfgang Ashley
Visualization: Aaron Wolfgang Ashley, Mainak Mookherjee
Writing – original draft: Aaron Wolfgang Ashley
Writing – review & editing: Aaron Wolfgang Ashley, Mainak Mookherjee, Man Xu, Tony Yu, Geeth Manthilake, Yanbin Wang

Volcanism is perhaps the most obvious and dramatic process involving geofluids. Yet these geofluids are generated deep within the Earth and other planetary interiors. Water-rich aqueous fluids are expected to be prevalent at gigapascal (GPa)-scale pressures in subduction zones, in which tectonic plates submerge into the mantle (Hacker, 2008; Hermann et al., 2006; Manning, 2004). Silicate melts are also prevalent in subduction zones where melting may begin at several GPa (Syracuse et al., 2010). The timescales of geofluid extraction and ascent, that is, mobilization, from source regions are strongly dependent on the geofluid viscosity (Stolper et al., 1981). Production of magmas is also influenced by the viscosities of mixing melts (Laumonier et al., 2014). At high pressures, water-rich fluids and silicate melts may also become miscible as a supercritical fluid (Bureau & Keppler, 1999; Mibe et al., 2008; Shen & Keppler, 1997). Such supercritical fluids may display an enhanced ability to dissolve rock compared to other geofluids (Kessel, Schmidt, et al., 2005; Kessel, Ulmer, et al., 2005). The viscosity of supercritical fluids may therefore significantly influence mass/energy transport in subduction zones (Audétat & Keppler, 2004).

Geophysical observations indicate that melts exist throughout the Earth's interior, including the lithosphere-asthenosphere boundary (Naif et al., 2013), upper mantle (Eilon & Abers, 2017; Key et al., 2013), mantle transition zone and lower mantle (Revenaugh & Sipkin, 1994; Schmandt et al., 2014; Tauzin et al., 2010), core mantle boundary (Ross et al., 2004; Rost et al., 2005; Vidale & Hedlin, 1998), and the outer core. These geophysical observations are generally lowered seismic velocities and/or enhanced electrical conductivities. Partial melting occurs when the melting temperatures of source rocks are lower than the expected temperature profile with depth into the Earth, that is, the geothermal gradient. Such conditions could arise when the geothermal gradient changes slope or when melting temperatures are lowered due to volatiles (Schmandt et al., 2014). Thus, it is crucial to constrain the viscosities of melts at high pressures and temperatures relevant for the Earth's interior.

Our understanding of the formation of the modern mantle is also critically dependent on high-pressure constraints of melt viscosities. Planetary-scale impact collisions may have melted much of the early mantle into a “magma ocean” (Abe, 1997; Elkins-Tanton, 2012; Schaefer & Elkins-Tanton, 2016). Cooling and solidification of the modern mantle from this magma ocean is directly tied to convection which is influenced by the magma viscosity (Bajgain et al., 2022; Karki & Stixrude, 2010; Zeff & Williams, 2019). The viscosity of the magma ocean would have also influenced sinking droplets of iron-nickel alloys that would ultimately form the core of the Earth below the mantle. The formation of an iron core would result in a magnetic geodynamo that shields the Earth from solar radiation. The modern geodynamo is driven by the convection of the liquid outer core and is influenced by the viscosity of the liquid alloy (Zhu et al., 2022).

Given the importance of geofluids at depth in planetary interiors, it is key that we constrain their viscosities at relevant pressure and temperature conditions. However, measuring the viscosity of geofluids at high pressures relevant for planetary interiors is experimentally challenging. Generating high pressures requires carefully designed devices, including cold-seal or internally heated pressure vessels (collectively referred to here as CS/IH-PV), piston cylinder devices, multi-anvil presses, Paris-Edinburgh devices, or diamond-anvil-cells. Classic viscometry methods, such as capillary flow, rotatory, oscillatory, parallel-plate, or (micro)penetration, are not easily compatible with these high-pressure devices. High pressure viscometry has instead relied on the falling sphere technique as only a small sphere must be added into the central chamber of the high-pressure device. The sphere will sink (or float) due to its higher (or lower) density than the surrounding fluid. Stokes' Law describes an inverse relationship between the sphere velocity and the viscosity of the fluid. Hence, Stokes' Law can be used to calculate the fluid viscosity from the velocity of the moving sphere. The sphere velocity can be estimated either by *ex situ* measurement of the sphere displacement (Shaw, 1963) or by in situ observation using X-ray radiography (Kanzaki et al., 1987) or optical methods (King et al., 1992). Notably, the falling sphere method has also been extensively used in broader material sciences at ambient pressures due to its relative simplicity. The production and use of metal alloys, aluminosilicate glasses, polymers, varnishes, cosmetics, food products, and suspensions depends strongly on their viscosities (Brizard et al., 2005; Zhang & Chou, 2012). Falling sphere viscometry is therefore very useful for measuring the viscosities of a wide variety of materials across a range of pressure and temperature conditions.

Critically, evaluation of the falling sphere method found additional drag acting on the sphere due to boundary effects from the finite size of a sample container (Brizard et al., 2005; Faxén, 1922; Fidleris & Whitmore, 1961; Flude & Daborn, 1982; Francis, 1933; Ladenburg, 1907; Lorentz, 1907; Sutterby, 1973; Tanner, 1963). This

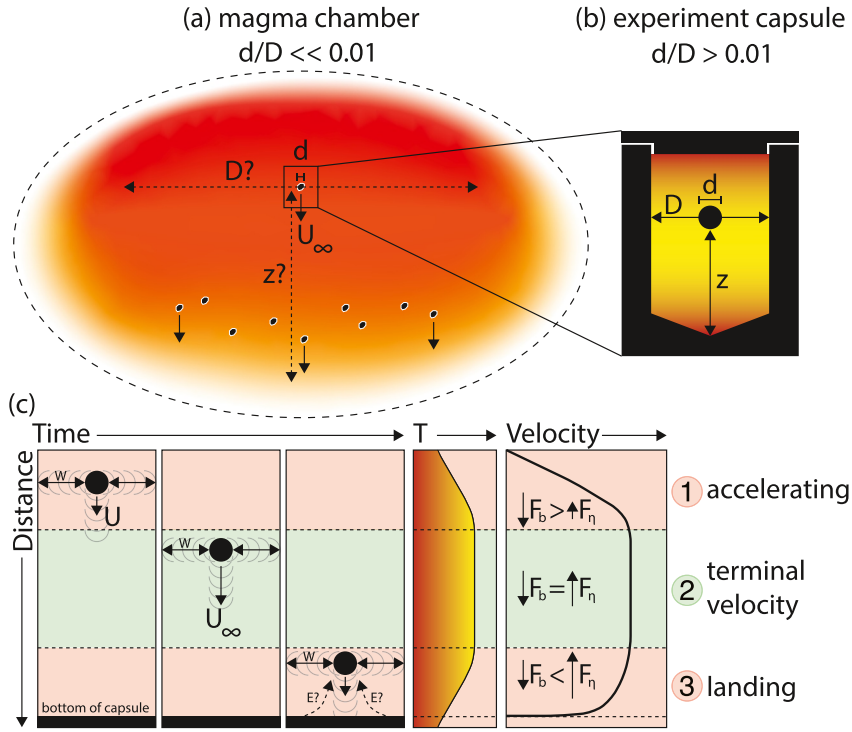

Figure 1. Schematic overview of Stokes' Law in a large volume, such as a magma chamber (a), versus the finite size of a typical experimental capsule. (c) Schematic illustration of a falling sphere experiment. From left to right, three panels show a falling sphere which experiences drag due to the capsule walls, that is, W, and drag due to the bottom of the capsule, that is, E. The symbol U indicates velocity and U_∞ indicates terminal velocity. The fourth panel from the left shows a possible temperature profile for an experiment. The fifth panel illustrates the velocity profile during sinking of the sphere. Three regimes are recognized and color-coded throughout the panels. The sphere starts to sink by acceleration due to gravity. The negative buoyancy (sinking) force due to gravity, that is, F_b, is greater than the viscous drag force, that is, F_η. As the forces balance, the sphere sinks under constant, terminal velocity. As the sphere approaches the bottom of the capsule, it may begin to slow due to a combination of cooling temperatures and/or increasing end-effect drag. As such F_η begins to exceed F_b.

additional drag is not captured in the traditional form of Stokes' Law and must be corrected (Figure 1). Decreasing the size of the container relative to the sphere enhances the additional drag acting on the sphere. As a result, the drag becomes significant in high-pressure experiments as very small capsules are required by the devices used to generate high pressure (Figure 1). Multiple correction schemes have been proposed and discussed in detail to account for the additional drag effects (Brizard et al., 2005). However, there is no clear consensus regarding the most appropriate correction scheme to use in high-pressure experiments (Tables 1–4, full compilation in Table S1). In this study, we review in detail the application of Stokes' Law at high pressures and the schemes used to account for drag. To better understand the current corrections for drag acting on Stokes' Law, we conducted high-pressure falling sphere experiments in a multi-anvil press on aluminosilicate melts. We apply the results from our experiments to identify the most appropriate scheme from existing equations for high pressure research. Further, we apply this work to better understand inherent uncertainties for falling sphere viscometry in various devices which are used to recreate conditions relevant to planetary interiors.

2. Application of Stokes' Law

2.1. Principles of Stokes' Law

Before considering the various correction schemes for falling sphere viscometry, it is helpful to review the fundamental principles underlying Stokes' Law. In an ideal scenario, a small particle sinks in an infinitely large fluid reservoir. As such, the reservoir boundaries do not significantly influence the viscous flow around the particle. An example may be a crystal sinking in a large magma chamber or ocean (Figure 1). The crystal experiences a negative buoyancy force when it is denser than the surrounding melt. The crystal may also float or rise when it is less dense than the melt (Secco, 1994; Zhu et al., 2022). Assuming the crystal is spherical, it will sink (or

Table 1
Compilation of High-Pressure Falling Sphere Experiments Which Used Piston Cylinder Devices

Reference	Exp. approach[a]	Applied correction[b]	P (GPa)[c]	T (K)[c]	$\log_{10}U$ (μm s^{-1})[c]	d (μm)[c]	d/D[c]	z_{H_c} (mm)[c]	$\log_{10}\eta$ (Pa s)[c]
Rhyolitic ± H_2O									
Shaw (1963)	1x?	W	0.1 to 0.2	973 to 1173	NR	500 to 800	0.2 to 0.32[e]	10	4.2 to 5.5
Baker and Vaillancourt (1995)	1x?	WE_L	1	1073 to 1273	−1.1 to 0.9	147 to 314	0.05 to 0.1[e]	3 to 4	1.9 to 4.1
Ardia et al. (2008)	1x	W	0.5 to 2.5	854 to 1628	−1.2 to 0.7	214 to 413	0.05 to 0.12[e]	4 to 6	3.6 to 6.9
(Na, K)$AlSi_3O_8$ ± H_2O ± CO_2 ± $CaMgSi_2O_6$									
Kushiro (1978)	1x	W	0.5 to 2	1673	−0.7 to 0.4	760 to 1040	0.2 to 0.3[e]	10	3.3 to 3.9
Brearley et al. (1986)	4 to 6x	W	1.0 to 2.5	1773 to 1873	NR	NR	NR	NR	−0.4 to 2.3
Dingwell (1987)	1 to 2x	W	0.25 to 2.25	1273 to 1873	−0.6 to 1.2	200 to 334	0.04 to 0.07[e,f]	10[f]	1.3 to 3.6
Brearley and Montana (1989)	1 to 4x	W	1.5 to 2.5	1673	−0.3 to 0.3	80 to 270	0.05 to 0.15[d]	10	3.5 to 4.0
White and Montana (1990)	1x	W	1.5 to 2.5	1773 to 1873	0.09 to 1.2	168 to 512	0.06 to 0.17[d]	NR	1.3 to 3.4
Andesitic									
Kushiro et al. (1976)	1 to 2x	W	0.75 to 2	1523 to 1623	−0.1 to 1.3	420 to 590	0.08 to 0.2[e]	1	1.9 to 2.5
Dunn and Scarfe (1986)	2 to 5x	W	0.35 to 2	1623	0.05 to 0.9	103 to 300	0.03 to 0.06[f]	10[f]	2.1 to 2.7
$NaAlSi_2O_6$									
Kushiro (1976)	1x	W	0.5 to 2.4	1623	0.07 to 1.1	800 to 910	0.15 to 0.16[d,e]	10	2.7 to 3.6
Basaltic									
Kushiro et al. (1976)	1 to 2x	W	1 to 3	1623 to 1773	0.5 to 1.4	377 to 737	0.3 to 0.5[e]	10	−0.1 to 0.6
(Ca,Mg)(Mg,Fe)Si_2O_6									
Brearley et al. (1986)	4 to 6x	W	0.5 to 1.5	1773	NR	NR	NR	NR	−0.5 to 0
Ca-K-Mg-Al-Si-O or K-Si-O									
Dickson et al. (1990)	3 to 5x	W	0.5 to 2.4	1473	NR	NR	NR	NR	1.2 to 1.9

[a]"Experimental (Exp.) approach" describes the number of spheres typically used in the study and the capsule design. "Trap" indicates that spheres were released into the melt using a phase more refractory than the target sample (Liebske et al., 2005; Terasaki et al., 2001, 2002, 2006). The more typical approach fills the sample capsule entirely with one target phase. Studies tagged with "*N*x and Trap," where *N* is the number of spheres, indicate that both typical and trap approaches were used. "Float" indicates that a sphere less dense than the melt was allowed to ascend for the measurement (Secco, 1994). [b]The "Applied Correction" describes the form of Stokes' Law used to calculate the reported viscosities. Abbreviations R, W, and WE indicate the uncorrected or raw Stokes' Law equation, the corrected equation for wall effects only, and the corrected equation for wall and end effects combined. Subscripts L and M indicate the end effect schemes by Ladenburg (1907) and Maude (1961), respectively. The "A" refers to an additional correction for non-spherical grains (Mori et al., 2000) that is not discussed in the current study. [c]Abbreviations are P for pressure, T for temperature, U for sphere velocity, d for sphere diameter, d/D for sphere-to-capsule diameter ratio, z_{H_c} for the maximum possible falling distance, often referred to as H_C or sample height in the literature, and η for viscosity. Other abbreviations are NR for not reported, FIG for value(s) shown in figure(s). [d]Recalculated from reported correction factors. [e]Estimated from explicitly reported dimensions of experimental geometry either in figure(s) or in text. [f]Value estimated from cited work and assumed to be the same.

float) according to the buoyancy force given by $F_b = \pi d^3 g \Delta\rho/6$, where d is the crystal diameter (m), g is the acceleration due to gravity (9.81 m s^{-2} for Earth), and $\Delta\rho$ is the density contrast between the sphere and melt (kg m^{-3}) (Figure 1). Acceleration may also be provided by a centrifuge (Ardia et al., 2008). The melt exerts an opposing viscous drag force on the sinking crystal given by $F_\eta = 3\pi d\eta U$, where η is the viscosity of the melt (Pa s) and U is the velocity of the crystal (m s^{-1}). When the two forces balance, that is, $F_b = F_\eta$, the crystal discontinues acceleration and travels under constant terminal velocity, that is, U_∞. The force balance yields Stokes' Law,

Table 2
Compilation of High-Pressure Falling Sphere Experiments Which Used Multi-Anvil Devices

Reference	Exp. approach[a]	Applied correction[b]	P (GPa)[c]	T (K)[c]	$\log_{10}U$ (μm s^{-1})	d (μm)[c]	d/D[c]	z_{H_c} (mm)[c]	$\log_{10}\eta$ (Pa s)[c]
Carbonate(-rich)									
Dobson et al. (1996)	2x	R and W	2.5 to 5.5	803 to 1773	2.8 to 4.4	30 to 290	0.02 to 0.15[d]	4[d]	−2.2 to −0.8
Ca-K-Mg-Al-Si-O or K-Si-O									
Allwardt et al. (2007)	2x Trap	W	3.7 to 5.5	1913 to 2013	−0.3 to −0.5	70 to 83	0.05 to 0.06[f]	3.4[f]	−0.4 to −0.7
Suzuki (2019a)	1x	W	1.3 to 7.4	1583 to 2133	NR	NR	NR	2[g]	−0.6 to 0.8
$NaAlSi_3O_8 \pm H_2O$									
Mori et al. (2000)	1x	W + A	3 to 7	2000	0.2 to 1.1	<162	0.05 to 0.1[h]	NR	−0.004 to 0.7
Suzuki et al. (2002)	1x	W	2.6 to 5.3	1873 to 1973	0.6 to 1.5[h]	100 to 140	0.18[d]	2[d]	0.3 to 1.2
Funakoshi et al. (2002)	1x	W	2.1 to 5.2	1973	1.1 to 1.9[h]	100 to 170[d]	0.08 to 0.1[f]	2	0.4 to 1.2
Poe et al. (2006)	1x	W	2.5	1823 to 1923	0.7 to 1.5	<200	0.1[f]	3.5	1.2 to 2.1
Dacitic $\pm H_2O$									
Tinker et al. (2004)	1x	W	1.5 to 7.1	1730 to 1950	0.1 to 2.5	90 to 300	0.05 to 0.17[f]	1.6	−0.2 to 1.9
Melilitic									
Suzuki (2019b)	1x	W	1.2 to 5.6	1573 to 1948	NR	150[d]	0.1[d,f]	2[g]	−0.2 to 0.9
$NaAlSi_2O_6 \pm CO_2$									
LeBlanc and Secco (1995)	1x	WE_L	2.4 to 2.9	1623 to 1723	FIG	700 to 740	0.3 to 0.4[d,f]	3 to 5[d]	3.3 to 4.8
Suzuki et al. (2011)	1x	W	1.6 to 5.4	1623 to 2153	−0.2 to 2	NR	NR	2[g]	−0.05 to 2.4
Suzuki (2018)	1x	W	2.1 to 3.5	1553 to 1693	NR	NR	NR	2[g]	−0.9 to 1.2
$(Ca, Mg)(Mg, Fe)Si_2O_6 \pm NaAlSi_2O_6$									
Reid et al. (2003)	1 and 2x	WE_L	3.5 to 13.1	2000 to 2470	2.7 to 3.7	100 to 147	0.1[d]	2.3[d]	−1.6 to −0.3
Suzuki et al. (2005)	1x	W	1.88 to 7.9	2003 to 2173	FIG	65 to 135	0.06 to 0.14[f]	2[g]	−0.6 to 0.5
Edwards (2019)	Trap	WE_L	10^{-4} to 7.2	1514 to 2133	0.6 to 3.1	77 to 166	0.04 to 0.2[f]	0.5 to 1.8[f]	−1.3 to 1.5
Xie et al. (2020)	1x	WE_L	4.8 to 30	2203 to 3250	3 to 3.7	65 to 144	0.1 to 0.3[d]	0.8[d] to 1	−2.0 to −1.2
Basaltic									
Sakamaki et al. (2013)	1x	W	0.85 to 6.51	1850 to 2100	FIG	100 to 140	0.18[d,g]	2[d,g]	−0.8 to 0.06
Peridotitic or $(Mg, Fe)_2SiO_4$									
Liebske et al. (2005)	Trap	W	2.8 to 13	2043 to 2523	3.1 to 3.9	105 to 174	0.04 to 0.12[e]	2.3 to 3.4	−1.7 to −0.9
Xie et al. (2020)	1x	WE_L	5.7 to 29	2420 to 3000	2.8 to 3.6	59 to 130	0.1 to 0.3[d]	0.8[d] to 1	−1.7 to −1.3

Table 2
Continued

Reference	Exp. approach[a]	Applied correction[b]	P (GPa)[c]	T (K)[c]	$\log_{10}U$ (μm s^{-1})	d (μm)[c]	d/D[c]	z_{H_c} (mm)[c]	$\log_{10}\eta$ (Pa s)[c]
Xie et al. (2021)	1x	WE_L	7 to 25	2173 to 2773	3.1 to 3.3	59 to 80	0.1 to 0.2[d]	0.6 to 0.8[d]	0.2 to 0.6
Fe ± Ni ± S ± C									
Secco (1994)	1x? Float	WE_L	3 to 5	1498	NR	200 to 1000	0.07 to 0.35[d]	5.2	1.5 to 1.7
LeBlanc and Secco (1996)	1x	WE_L	2 to 5	1373 to 1573	NR	500[d]	0.25[d]	3.5[d]	0.09 to 1.7
Dobson et al. (2000)	1 to 2x	WE_L	0.5 to 5.5	1423 to 1980	3.2 to 4.2	44 to 500	0.06 to 0.3[e]	0.8[d] to 3.6[e]	−1.7 to −2.4
Urakawa et al. (2001)	1 to 3x	WE_L	5 to 7	1333 to 1373	3.3 to 3.5	100	0.06[d]	0.6 to 2[d]	−1.6 to −1.8
Terasaki et al. (2001)	Trap	WE_L	1.5 to 6.9	1253 to 1923	3.1 to 4.1	100 to 150	0.05 to 0.15[e]	0.2 to 1.2[e]	−2.1 to −1.4
Rutter, Secco, Liu, et al. (2002)	1x	WE_L	1.6 to 5.5	1823	3.4 to 3.6	400[d] to 530[e]	0.3[d] to 0.4[e]	2.5	−2.6 to −2.3
Rutter, Secco, Uchida, et al. (2002)	1x	WE_L	2.3 to 6.0	1823	FIG	NR	NR	NR	−2.6 to −1.8
Secco et al. (2002)	1x	WE_L	1.5 to 4	1463 to 1523	FIG	250 to 500	0.2 to 0.4[d]	2 to 4[d]	−4 to −2
Terasaki et al. (2002)	Trap	WE_L	2.8 to 7	1965 to 2173	NR	100 to 150	NR	NR	−2.4 to −1.6
Terasaki et al. (2004)	1x	WE_L	3.2 to 9.7	788 to 1067	2.1 to 2.7	93 to 122	0.06 to 0.09[e]	1[e] to 2[f]	−1 to −0.2
Terasaki et al. (2006)	1x and Trap	W	3 to 16	1605 to 1843	3.2 to 4.6	120 to 140	0.12 to 0.14[f]	NR	−2.5 to −2.1

[a]"Experimental (Exp.) approach" describes the number of spheres typically used in the study and the capsule design. "Trap" indicates that spheres were released into the melt using a phase more refractory than the target sample (Liebske et al., 2005; Terasaki et al., 2001, 2002, 2006). The more typical approach fills the sample capsule entirely with one target phase. Studies tagged with "*N*x and Trap," where *N* is the number of spheres, indicate that both typical and trap approaches were used. "Float" indicates that a sphere less dense than the melt was allowed to ascend for the measurement (Secco, 1994). [b]The "Applied Correction" describes the form of Stokes' Law used to calculate the reported viscosities. Abbreviations R, W, and WE indicate the uncorrected or raw Stokes' Law equation, the corrected equation for wall effects only, and the corrected equation for wall and end effects combined. Subscripts L and M indicate the end effect schemes by Ladenburg (1907) and Maude (1961), respectively. The "A" refers to an additional correction for non-spherical grains (Mori et al., 2000) that is not discussed in the current study. [c]Abbreviations are P for pressure, T for temperature, U for sphere velocity, d for sphere diameter, d/D for sphere-to-capsule diameter ratio, z_{H_c} for the maximum possible falling distance, often referred to as H_C or sample height in the literature, and η for viscosity. Other abbreviations are NR for not reported, FIG for value(s) shown in figure(s). [d]Estimated by measuring scaled figure(s), in combination with other reported values when available. Uncertainty may be significant if scale is inaccurate. [e]Recalculated from reported correction factors. [f]Estimated from explicitly reported dimensions of experimental geometry either in figure(s) or in text. [g]Value estimated from cited work and assumed to be the same. [h]Numerically recalculated using least-square regression from other reported or estimated values.

$$\eta_R = \frac{gd^2\Delta\rho}{18U_\infty} \quad (1)$$

By using Stokes' Law, the viscosity of a liquid may be constrained by measuring U_∞ of a sphere with a known diameter. However, measurement of U_∞ in a laboratory setting requires a finite chamber to contain the liquid which deviates from the ideal scenario (Figure 1). Additional drag effects acting on the sphere are dependent on the finite container and Equation 1 must be modified (Brizard et al., 2005). We label Equation 1 using the subscript "*R*" to indicate the "raw" or uncorrected Stokes' Law for clarity.

2.2. Review of Correction Schemes

We find at least four different schemes to correct Stokes' Law have been most frequently adopted in prior high-pressure falling sphere experiments (Tables 1–4; Table S1). Broadly, the schemes aim to correct for drag due to

Table 3
Compilation of High-Pressure Falling Sphere Experiments Which Used CS/IH-PV Devices

Reference	Exp. Approach[a]	Applied correction[b]	P (GPa)[c]	T (K)[c]	$\log_{10}U$ (μm s^{-1})[c]	d (μm)[c]	d/D[c]	z_{H_c} (mm)[c]	$\log_{10}\eta$ (Pa s)[c]
Rhyolitic ± H_2O									
Schulze et al. (1996)	1 to 2x	W	0.3 to 1.0	1073 to 1673	−2 to 0.2	190 to 344	0.05 to 0.09[e]	16	2.5 to 4.9
SiO_2 + $NaAlSi_3O_8$ ± H_2O									
Holtz et al. (1999)	1x and 2x	W	0.2 to 0.4	1253 to 1648	−1.3 to −0.2	210 to 318	0.05 to 0.08[d]	15 to 18	2.8 to 4.0
Dacitic ± H_2O									
Whittington et al. (2009)	1x?	W	0.3	1373 to 1523	0.4 to 0.9	194	0.03[d]	11 to 17[f]	1.7 to 2.1
Andesitic ± H_2O									
Vetere et al. (2006)	2 to 3x	W	0.5	1323 to 1573	−0.5 to 1.3	95 to 500	0.01 to 0.1[d,e]	11 to 17	1 to 6
Vetere et al. (2008)	1 to 4x	W	0.2 to 2	1323 to 1573	0.1 to 1.4	94 to 880	0.01 to 0.07[d]	11 to 17[f]	0.7 to 3.1

[a]"Experimental (Exp.) approach" describes the number of spheres typically used in the study and the capsule design. "Trap" indicates that spheres were released into the melt using a phase more refractory than the target sample (Liebske et al., 2005; Terasaki et al., 2001, 2002, 2006). The more typical approach fills the sample capsule entirely with one target phase. Studies tagged with "*N*x and Trap," where *N* is the number of spheres, indicate that both typical and trap approaches were used. "Float" indicates that a sphere less dense than the melt was allowed to ascend for the measurement (Secco, 1994). [b]The "Applied Correction" describes the form of Stokes' Law used to calculate the reported viscosities. Abbreviations R, W, and WE indicate the uncorrected or raw Stokes' Law equation, the corrected equation for wall effects only, and the corrected equation for wall and end effects combined. Subscripts L and M indicate the end effect schemes by Ladenburg (1907) and Maude (1961), respectively. The "A" refers to an additional correction for non-spherical grains (Mori et al., 2000) that is not discussed in the current study. [c]Abbreviations are P for pressure, T for temperature, U for sphere velocity, d for sphere diameter, d/D for sphere-to-capsule diameter ratio, z_{H_c} for the maximum possible falling distance, often referred to as H_C or sample height in the literature, and η for viscosity. Other abbreviations are NR for not reported, FIG for value(s) shown in figure(s). [d]Recalculated from reported correction factors. [e]Estimated from explicitly reported dimensions of experimental geometry either in figure(s) or in text. [f]Value estimated from cited work and assumed to be the same.

(a) the sample capsule walls, (b), inertia of the falling sphere, (c) the ends of the capsule, that is, its top and bottom, or (d) some combination of schemes (a)–(c) (Figure 1). We consider each of the four schemes in detail to better understand the influence of the corrections on the calculated viscosity from Stokes' Law.

2.2.1. Correction for the Wall Effect

Nearly every previous high-pressure study corrected η_R for drag acting on the sphere from the capsule walls, also known as the wall effect (Tables 1–4; Table S1). The wall effect correction is given by

$$\eta_W = \eta_R \cdot \left[1 - 2.104\left(\frac{d}{D}\right) + 2.09\left(\frac{d}{D}\right)^3 - 0.95\left(\frac{d}{D}\right)^5\right] \quad (2)$$

where η_W indicates the viscosity corrected to the wall effect (W), d is the sphere diameter and D is the inner diameter of the capsule (Faxén, 1922). This scheme is also well known as the Faxén correction.

2.2.2. Correction for Inertia

The Stokes' Law formalism with the wall correction scheme, that is, Equation 2, can be expanded to account for drag due to inertia of the falling sphere in

$$\eta_{WI} = \eta_R \cdot \left[1 - \frac{3}{16}Re_n - \frac{d}{D}C + 2.09\left(\frac{d}{D}\right)^3 - 0.95\left(\frac{d}{D}\right)^5\right] \quad (3)$$

where the subscript WI indicates wall + inertia effect corrections, Re_n is the Reynolds number given by $Re_n = \rho_S U_\infty d/\eta$ and ρ_S is the sphere density (Brizard et al., 2005; Faxén, 1922). The C is a polynomial function of Re_n given by $C = f\left(\frac{Re_n/4}{d/D}\right)$ (Table S2 in Supporting Information S1). We found no reported instance in high-pressure research that used this form of Stokes' Law (Tables 1–4; Table S1). Instead, the Re_n and hence inertia terms were assumed or estimated to be negligibly small, which yields Equation 2 as Re_n approaches zero.

Table 4
Compilation of High-Pressure Falling Sphere Experiments Which Used Paris Edinburgh Devices

Reference	Exp. Approach[a]	Applied correction[b]	P (GPa)[c]	T (K)[c]	$\log_{10}U$ (μm s^{-1})[c]	d (μm)[c]	d/D [c]	z_{H_c} (mm)[c]	$\log_{10}\eta$ (Pa s)[c]
(Na, K)Cl									
Kono et al. (2013)	1x	WE_M	1.5 to 7.3	1273 to 2073	FIG	94 to 133	0.05 to 0.07	2	−2.8 to −2.6
Carbonate(-rich)									
Kono et al. (2014)	1x and Trap	WE_M	0.9 to 6.2	1633 to 2063	3.9 to 4.5	84 to 153	0.06 to 0.11[d]	1.1 to 1.6[d]	−2.2 to −2.0
Stagno et al. (2018)	1x and Trap	WE_M	1.7 to 4.6	1473 to 1973	4.1 to 4.3	38 to 135	0.03 to 0.11[e]	2	−2.6 to −2.1
Stagno, Kono, et al. (2020)	1x and Trap	WE_M	2.4 to 5.3	1838 to 2428	2.9 to 3.8	86 to 191	0.07 to 0.16[f]	2	−1.7 to −1.1
Melilitic									
Stagno, Stopponi, et al. (2020)	1x and Trap	WE_M	1 to 4.7	1538 to 2028	1.8 to 3	85 to 146	0.07 to 0.12[f]	2	−1.0 to 0.3
Mercurian basaltic-andesitic ± S									
Mouser et al. (2021)	1x	WE_M	2.6 to 6.2	1873 to 2273	1.1 to 2.7	120 to 220	0.08 to 0.15[e]	1.4 to 4[e]	−0.2 to 1.0
Basaltic									
Bonechi et al. (2022)	1x	WE_M	0.7 to 7.0	1608 to 2273	1.6 to 2.4	87 to 170	0.07 to 0.14	2	−0.3 to 0.5
Lunar mafic to ultramafic									
Dygert et al. (2017)	1x	WE_M	0.1 to 4.4	1573 to 1873	2 to 2.7	100 to 200	0.05 to 0.2[d]	1.9[d]	−0.7 to 0.2
Rai et al. (2019)	1x	WE_L	1.1 to 2.4	1830 to 2090	1.4 to 2.3	53 to 76	0.1 to 0.15[f]	1.5	−0.9 to −0.06
$(Ca, Mg)(Mg, Fe)Si_2O_6$									
Cochain et al. (2017)	1x	WE_L	1.0 to 7.6	1823 to 2243	FIG	108 to 186	0.1 to 0.2[f,g]	1.8[g]	−1.4 to 1.0
$(Mg, Fe)_2SiO_4$									
Spice et al. (2015)	1x	WE_L	1.3 to 9.2	1623 to 2123	3.4 to 3.9	108 to 185	0.09 to 0.15[f]	1[f]	−1.5 to −1.3
Fe ± Ni ± S ± C									
Kono et al. (2015)	1x?	WE_M	1.2 to 6.4	1523 to 2043	3.8 to 4.4	82 to 131	0.05 to 0.13[f]	2	−2.3 to −2.1
Zhu et al. (2022)	1x Float	WE_M	1.8 to 6.3	1973	FIG	250	0.25[f]	2	−2.3 to −1.4

[a]"Experimental (Exp.) approach" describes the number of spheres typically used in the study and the capsule design. "Trap" indicates that spheres were released into the melt using a phase more refractory than the target sample (Liebske et al., 2005; Terasaki et al., 2001, 2002, 2006). The more typical approach fills the sample capsule entirely with one target phase. Studies tagged with "*N*x and Trap," where *N* is the number of spheres, indicate that both typical and trap approaches were used. "Float" indicates that a sphere less dense than the melt was allowed to ascend for the measurement (Secco, 1994). [b]The "Applied Correction" describes the form of Stokes' Law used to calculate the reported viscosities. Abbreviations R, W, and WE indicate the uncorrected or raw Stokes' Law equation, the corrected equation for wall effects only, and the corrected equation for wall and end effects combined. Subscripts L and M indicate the end effect schemes by Ladenburg (1907) and Maude (1961), respectively. The "A" refers to an additional correction for non-spherical grains (Mori et al., 2000) that is not discussed in the current study. [c]Abbreviations are P for pressure, T for temperature, U for sphere velocity, d for sphere diameter, d/D for sphere-to-capsule diameter ratio, z_{H_c} for the maximum possible falling distance, often referred to as H_C or sample height in the literature, and η for viscosity. Other abbreviations are NR for not reported, FIG for value(s) shown in figure(s). [d]Estimated by measuring scaled figure(s), in combination with other reported values when available. Uncertainty may be significant if scale is inaccurate. [e]Recalculated from reported correction factors. [f]Estimated from explicitly reported dimensions of experimental geometry either in figure(s) or in text. [g]Value estimated from cited work and assumed to be the same.

2.2.3. Correction for the End Effect

Roughly half of previous high-pressure work combined the wall correction with a correction for drag due to the end(s) of the capsule (Tables 1–4; Table S1), known as the end effect. The end correction scheme alone is given by

$$\eta_E = \frac{\eta_R}{\left(1 + \frac{9}{8} \cdot \frac{d}{2z}\right)} \tag{4}$$

where the subscript E indicates the end effect correction (Lorentz, 1907). In development of a falling sphere viscometer, z was described as the distance between the sphere and the bottom of the capsule (Brizard et al., 2005).

Aside from DAC experiments (Audétat & Keppler, 2004), we note that Equation 4 is not the typical end correction which has been used in high-pressure research (Tables 1–4; Table S1). Previous studies have used one of two other variations on the end effect scheme. Many high-pressure articles refer to one scheme from a summary on high temperature viscometry by Kingery (1959), who reported it after Bacon (1936). The scheme is given by

$$\eta_{E_L} = \frac{\eta_R}{\left(1 + 3.3 \cdot \frac{d}{2H_C}\right)} \tag{5}$$

where H_C is described as the total height of the capsule. We note that Ladenburg (1907) originally proposed the scheme after considering drag acting on the sphere from the top and bottom of a vertical cylinder. For clarity, we designate this variation with the subscript E_L (Tables 1–4; Table S1).

Another version of the end effect scheme is given by Maude (1961) who evaluated the drag in context of two falling spheres moving at different rates after Stimson and Jeffery (1926). More recent work in high-pressure science (Kono et al., 2013) summarized the correction by

$$\eta_{E_M} = \frac{\eta_R}{\left(1 + \frac{9}{8} \cdot \frac{d}{2z} + \left(\frac{9}{8} \cdot \frac{d}{2z}\right)^2\right)} \tag{6}$$

where we use the subscript E_M for clarity (Tables 1–4; Table S1). We note this variation of the end correction was originally described as a power series expansion (Maude, 1961), but higher order terms have not been recently included. We find ambiguity in the meaning of z in Equation 6. Despite the similarity of Equations 4 and 6, z in Equation 6 has been described as the "sample height" (Kono et al., 2013), that is, H_C as in Equation 5. We will evaluate the exact meaning of z using results from our own experiments in a later section.

2.2.4. Combining Correction Schemes

Combining the wall and end correction schemes yields

$$\eta_{WE} = \eta_R \cdot \frac{C_W}{C_E} \tag{7}$$

where C_W designates the wall scheme, that is, $[1 - 2.104(d/D) + 2.09(d/D)^3 - 0.95(d/D)^5]$, and C_E designates the end correction term as in Equations 4–6 (Tables 1–4; Table S1). For example, C_E from Equation 4 would be $(1 + 9d/16z)$. If we consider drag due to inertia of the falling sphere, the combined schemes may be given by

$$\eta_{WIE} = \eta_R \cdot \frac{C_{WI}}{C_E} \tag{8}$$

where C_{WI} indicates the wall and inertia correction schemes, that is, $[1 - 3Re_n/16 - d/DC + 2.09(d/D)^3 - 0.95(d/D)^5]$ as described in Equation 3.

2.2.5. Other Correction Schemes

The four major schemes outlined above are not comprehensive to those used in high-pressure research. Correction for the shape of non-spherical grains has also been applied when using diamonds instead of metallic spheres (Mori et al., 2000) and for spheres which deformed during the experiments (Holtz et al., 1999). In the latter case, it is likely that the spheres contained voids and collapsed during compression. Correction for the shape of the spheres is not widespread based on our review (Tables 1–4; Table S1). We also note that the shape-correction and the four schemes above have been applied in vertical cylinders, that is, the sphere falls along the longitudinal axis of the cylinder. The vertical cylinder is the most frequently used geometry in both ambient- and high-pressure devices for falling sphere viscometry (Brizard et al., 2005) (Tables 1–4; Table S1). However, horizontal cylinders have been used in diamond-anvil-cells (DAC) to study fluids that are challenging to solidify at ambient pressures/temperatures, that is, volatile-rich vaporous or supercritical fluids (Abramson, 2007, 2009; Abramson & West-Foyle, 2008; Audétat & Keppler, 2004; King et al., 1992). The horizontal technique has also been applied in a multi-anvil press to identify changes in rheology during melting (Pierru et al., 2022). In a horizontal cylinder, the sphere falls perpendicular to the longitudinal axis and between two parallel walls, that is, the ends of the cylinder. These walls would be the diamond culet faces in DAC experiments. The cylinder may also be tilted so that the sphere rolls along one wall. The change in orientation of the cell requires different consideration of the drag effects acting on the sphere (Audétat & Keppler, 2004). For brevity, we focus our review on the application of Stokes' Law in a vertical cylinder when using fully spherical particles or markers.

2.2.6. Previous Application of the Corrections

The dominant correction schemes applied in high-pressure research are the wall and end corrections (Tables 1–4; Table S1). The wall correction scheme (Equation 2) was first used at high-pressures in the seminal work by Shaw (1963) (Figure S1 in Supporting Information S1). Subsequent high-pressure experiments followed his method and applied the wall scheme well into recent years. In contrast, the combined wall and end correction schemes were not used until the 1990's (Figure S1 in Supporting Information S1). We suspect that significant time was required to disseminate the different correction schemes for Stokes' Law into high-pressure research. The work by Shaw (1963) came four decades after earlier consideration of drag effects by the capsule walls (Faxén, 1922). The combined wall and end correction schemes also came three decades after viscometry method articles which included equations for η_{WE} (Kingery, 1959; Maude, 1961). We notice that the use of the combined correction schemes has gradually become more common in high-pressure research (Figure S1 in Supporting Information S1). However, we have not found detailed discussion on whether the combined schemes are more appropriate than the wall scheme for high-pressure research. In contrast, materials science at ambient pressures has suggested that combining the schemes may not be necessary or suitable (Brizard et al., 2005).

We also find no obvious relationship between correction schemes and high-pressure devices. Piston cylinder devices were used for the first high-pressure viscosity measurements and hence coincide with use of the wall correction scheme (Table 1; Figure S1 in Supporting Information S1). The piston cylinders were gradually replaced by multi-anvil devices starting in the 1990's. The first multi-anvil experiments applied the combined wall and end correction schemes (Table 2). However, we also note that multi-anvil studies have used both the wall scheme and the combined schemes equally (Figure S1 in Supporting Information S1). In more recent years, Paris Edinburgh devices have become very common for high-pressure viscometry alongside multi-anvil devices. We notice that the Paris Edinburgh studies have exclusively used the combined wall and end correction schemes (Table 4). However, there is no obvious indication that this is advantageous for the device. We suspect this trend is instead due to the increased use of the combined schemes in previous multi-anvil work (Figure S1 in Supporting Information S1) and the first Paris-Edinburgh-based study which set the standard for subsequent work (Table 4). Indeed, as each experimental device generally uses a cylindrical sample chamber, the same physical considerations of a sinking sphere may be broadly applicable. Despite this, we are still lacking a critical evaluation of the available correction schemes for any high-pressure experiment.

3. Methods: Multi-Anvil Experiments

To examine the influence of the correction schemes on the viscosity of a fluid, we conducted high-pressure experiments using anhydrous aluminosilicate melt with an albite stoichiometry ($NaAlSi_3O_8$). Albitic melt is an analog for aluminosilicate-rich magmas which are crucial in the production of continental crust. The viscosity of

albitic melt at high pressures has been extensively studied (Bajgain & Mookherjee, 2020; Behrens & Schulze, 2003; Brearley & Montana, 1989; Brearley et al., 1986; Dingwell, 1987, 1995; Funakoshi et al., 2002; Holtz et al., 1999; Kushiro, 1978; Mori et al., 2000; Poe et al., 1997, 2006; Suzuki et al., 2002). These previous studies consistently show that the viscosity of albitic melt decreases with compression to at least 4–5 GPa. The decrease in viscosity at high pressures provides an advantage in promoting sinking of the sphere during our experiments. Furthermore, we can directly compare our results to an already extensive database (Tables 1 and 2; Table S1).

Our starting material was anhydrous albitic glass synthesized from fusing Na_2CO_3, $Al(OH)_3$, and SiO_2 reagent-grade powders in a 1:2:6 M ratio at ambient pressure in a 2000 K furnace at the Laboratoire Magmas et Volcans (LMV) at Blaise Pascal Clermont Ferrand II University, France. We crushed, powdered, and melted the glass repeatedly at ambient pressure to homogenize the mixture and remove volatiles. We examined powder from the glass for water contents using an Attenuated Total Reflectance module with a Hyperion-1000 Bruker Fourier Transform Infrared (FTIR) microscope at Florida State University (FSU). The absence of FTIR modes in the hydroxyl region (~3,000–4,000 cm^{-1}) confirms that the starting glass is anhydrous (Figure S2 in Supporting Information S1).

Derivation of Stokes' Law assumes a perfect sphere sinks in a melt or fluid (Section 2.1). Non-spherical geometries may introduce additional drag effects which must be considered with the boundary effects (Mori et al., 2000). To maintain a spherical form, the material for the spheres should be non-reactive and more refractive than the sample. A strong density contrast also helps to promote sinking. Previous experiments on albitic melt used platinum spheres as Pt is denser and relatively resistant to reaction with silicate melt (Funakoshi et al., 2002; Suzuki et al., 2002). Yet the previous experiments targeted ~2000 K to surpass the albite melting curve and ensure a fully molten state (Anovitz & Blencoe, 1999; Boyd & England, 1963; Gaudio et al., 2015; Shimada, 1972; Tenner et al., 2007). We note this temperature approaches the melting curve of Pt below 4 GPa (Anzellini et al., 2019; Belonoshko & Rosengren, 2012; Kavner & Jeanloz, 1998; Mitra et al., 1967) (Figure S3 in Supporting Information S1). To ensure the sphere does not melt with the albitic glass, we also considered rhenium as its melting curve is nearly 2000 K greater at any pressure than that for anhydrous albite (Burakovsky et al., 2018; Yang et al., 2012).

To ensure a strong density contrast between the sphere and melt, we examined the densities of Pt (Zha et al., 2008) and Re (Ono, 2022) at relevant pressure-temperature conditions for our experiments (Figure S4 in Supporting Information S1). We compared the densities of the metals to that of albitic melt under the same conditions. Previous studies on albitic melt viscosities (Funakoshi et al., 2002; Suzuki et al., 2002) estimated the density of the melt using a third-order Birch Murnaghan (BM3) equation of state, given by:

$$P = \frac{3}{2}K_{0T}\left[\left(\frac{\rho}{\rho_{0T}}\right)^{\frac{7}{3}} - \left(\frac{\rho}{\rho_{0T}}\right)^{\frac{5}{3}}\right]\left[1 - \frac{3}{4}(4 - K'_T)\left(\left(\frac{\rho}{\rho_{0T}}\right)^{\frac{2}{3}} - 1\right)\right] \quad (9)$$

where P is pressure (GPa), T indicates a reference temperature, ρ is the density of the melt at high pressure (g cm^{-3}), ρ_{0T} and K_{0T} are the zero-pressure melt density and bulk modulus (GPa) at T, respectively, and K'_T is the pressure derivative of K_{0T}. We note that a Vinet-type equation of state can also describe the density of albitic melt (Neilson et al., 2016). The BM3 equation of state does not include temperature dependence. Instead, the separate ρ_{0T}, K_{0T}, and K'_T terms are estimated at each temperature relevant to the experiment. The ρ_{0T} and K_{0T} of the melt are estimated using volumetric data for oxide components of the melt (Lange, 1997; Lange & Carmichael, 1987; Ochs & Lange, 1997) and ultrasonic measurements on sodic aluminosilicate melts (Kress et al., 1988), respectively. Previous viscosity work tested a range of K'_T from 4 to 8 as they did not have constraints on K'_T for albitic melt (Suzuki et al., 2002). More recently, *first-principles* molecular dynamics (FPMD) simulations explored the elastic properties of albitic melt at high pressures and temperatures (Ashley et al., 2022; Bajgain & Mookherjee, 2020; Kobsch & Caracas, 2020). These simulations constrain K'_T along several isotherms and predict that K'_T increases at higher temperatures (Table S3 in Supporting Information S1). We tested the effect of K'_T on the ρ of albitic melt by varying K'_T between 4 and 8 (Suzuki et al., 2002) and extrapolating K'_T predicted from FPMD (Figure S4 in Supporting Information S1). At temperatures relevant for our experiments, that is, ~2000 K, we find that the range in K'_T produces increasing uncertainty in the melt density with increasing pressure. However, the variation in the density due to K'_T is no more than ~0.2 g cm^{-3} at 10 GPa (Figure S4 in Supporting

Information S1). Previous work explored albitic melt viscosity to ≤7 GPa. Hence the choice in K'_T should not strongly affect the density contrast at conditions relevant for our experiments. We note that the K'_T predicted from FPMD is 5.0 ± 0.4 at 2000 K, in good agreement within the assumed K'_T range (Figure S4 in Supporting Information S1). We hence used the trend in K'_T predicted from FPMD to estimate the melt density more precisely for our experiments.

At the pressure-temperature conditions explored in this study, Pt and Re are significantly denser than albitic melt (Figure S4 in Supporting Information S1). Although Re is less dense than Pt, both metals are >17.8 g cm^{-3} denser than the melt. Hence, either metal will display a strong negative buoyancy in the melt at high pressures and temperatures. For our experimental study, we selected Re since it has higher melting temperatures. We created Re microspheres of less than 0.5 mm in diameter by arc melting a small filament of the metal (<1 mm in diameter).

We conducted the falling sphere experiments using the 1000-ton multi-anvil press frame with a T-25 Kawai-type module at the GSECARS 13-ID-D beamline at the Advanced Photon Source (APS), Argonne National Laboratory (Tinker et al., 2004; Wang et al., 2009). In the experimental hutch, the X-ray beam position is fixed. The press frame is mounted on a motorized table with five degrees of freedom and a positioning accuracy within 0.01 mm. Two modes are used in each experiment. A diffraction mode allows collection of energy dispersive X-ray diffraction patterns on the pressure standard and the sample to determine its physical state. An imaging mode allows collection of X-ray radiographic images. The diffraction mode collimates the incident and diffracted X-ray beams to a cross-section 0.1 by 0.1 mm in area. The 2θ angle is fixed at 6°. The intersection of the incident and diffracted beams defines the diffraction volume with the longest dimension parallel to the incident beam. The imaging mode is operated separately from the diffraction mode. Switching to imaging mode removes the entrance slits and illuminates the sample using the entire X-ray beam. The absorption contrast between the sphere and silicate melt is captured by converting the beam into visible light using a single-crystal of Ce-doped yttrium-aluminum-garnet (YAG) phosphor on the downstream side of the press. The visible light is reflected into a video camera through an optical lens to record a sequence of separate radiographic images. The radiographic images are used to track the position of the falling spheres through time (Kanzaki et al., 1987).

For each high-pressure experiment, we used 14/8 COMPRES multi-anvil assemblies (Leinenweber et al., 2012), that is, spinel-doped MgO octahedral pressure media with a 14 mm edge length combined with 25.4 mm tungsten-carbide anvils that have an 8 mm truncation edge length (TEL) (Figure S5 in Supporting Information S1). We packed albitic glass powder into a graphite capsule and created a small indentation in the center of the powder. We placed one Re microsphere into the indentation and covered the sphere with powder. We assured that enough glass powder was packed between the sphere and capsule to prevent contact between the two. If the sphere and capsule were to make contact, surface tension would prevent the sphere from falling. The inner height and diameter of the graphite capsules before compression were 1.8 and 1.6 mm, respectively. We used spheres <500 μm in diameter and varied the sphere sizes to examine the influence of drag on the settling of the spheres (Table 5). We also varied the vertical position of the spheres to examine the influence of end effect drag on the settling. We placed the graphite capsule into a sleeve of crushable alumina to shield it from the assembly furnace. We used a stepped graphite heater to minimize thermal gradients in the sample capsule (Leinenweber et al., 2012). We heated the assembly using resistive heating by a direct current power supply and monitored the temperature using Type-C tungsten-rhenium thermocouples placed above the sample center (Figure S5 in Supporting Information S1). Despite using a stepped heater, we note that the measured temperature at the thermocouples will be a minimum value and will increase toward the center of the assembly. We estimated the temperature at the center of the assembly using numerical modeling (Hernlund et al., 2006). Our analysis indicates that the temperature at the center is ∼50 K higher than recorded at the thermocouple junction. We determined the pressure by placing a disc of compacted MgO and h-BN powders in a 3:1 weight ratio directly above sample capsule and by constraining the equation of state of the MgO pressure marker using X-ray diffraction (Tange et al., 2009). We estimate the uncertainty in pressure to be ±0.5–0.7 GPa. No corrections were made for the effect of pressure on the thermocouples.

For each experiment, we compressed the assembly to a load of 100 tons without heating. Despite the same load, the cell assembly pressures varied slightly between experiments (Table 5). This pressure difference is attributed to small variations in each experiment cell assembly (Leinenweber et al., 2012). At the target load, we heated the

Table 5
Summary of Experiments in This Study

Experiment number	T2745	T2824
Input parameters		
Pressure (GPa)	3.1 ± 0.5	1.3 ± 0.7
Measured Temperature (K)	2073 ± 6	1871 ± 4
Sphere density, ρ_S (g cm^{-3})[a]	21.40 ± 0.05	21.44 ± 0.06
Melt density, ρ_M (g cm^{-3})[a]	2.59 ± 0.04	2.43 ± 0.07
Final capsule height, H_C (μm)[b]	1020 ± 50	1300 ± 100
Final capsule diameter, D (μm)[b]	1350 ± 10	1130 ± 60
Sphere diameter, d (μm)[c]	430 ± 3	127 ± 1
Average z (μm)[d]	40 ± 10	90 ± 20
Minimum z (μm)[d]	21	65
Maximum z (μm)[d]	53	132
Terminal velocity, U_∞ (μm s^{-1})	40 ± 2	5.43 ± 0.09
d/D	0.319 ± 0.003	0.113 ± 0.006
$2z/d$	0.19 ± 0.08	1.4 ± 0.4
Calculated viscosity (Pa s)		
Uncorrected, η_R (Equation 1)	48 ± 2	30.8 ± 0.8
Wall effect correction, η_W (Equation 2)[e]	18.870 ± 0.790	23.556 ± 0.662
Wall + inertia corrections, η_{WI} (Equation 3)[e]	18.889 ± 0.791	23.561 ± 0.662
End effect correction, η_E (Equation 4)[f]	7.4 ± 1.7	17.8 ± 1.8
Wall + end corrections, η_{WE} (Equation 7)[e]	2.918 ± 0.684	13.386 ± 1.389
Wall, inertia + end corrections, η_{WIE} (Equation 8)[e]	2.921 ± 0.685	13.389 ± 1.390

Note. Uncertainties are given as ±1 standard deviation. [a]Reported sphere and melt densities are average values from the Monte Carlo simulations which included randomly varied fitting parameters from equations of state (Section 3) and our experiment temperature and pressure data. [b]The final capsule heights and diameters were measured using back scatter electron (BSE) photomicrographs after the experiments (Figure S6 in Supporting Information S1). The post-experiment assemblies are assumed to largely preserve their geometries from the peak experiment conditions. [c]The sphere diameters were measured using BSE photos before the experiments. No correction was made for compression of the sphere volumes. [d]The z is the distance between the sphere and the bottom of the capsule, that is, the end of the fall. [e]Accounting for drag due to inertia of the falling sphere in our experiments results in ≤0.1% change in the mean viscosity compared to the wall term. Significant figures are expanded to show difference in values. Note that the inertia effect increases with settling velocity and decreasing melt viscosity (Figure 4). [f]Rounding the values following significant figures of the uncertainty, that is, 7 ± 2 and 18 ± 2 for T2745 and T2824, indicates greater uncertainties of ∼29% and 11%. Maintaining more digits shows that the uncertainties in the end correction alone rival that of the combined wall and end corrections, that is, ∼24% and 10%, respectively. See Figure 5 for visual comparison.

assembly incrementally below the melting curve of anhydrous albite (Figure S3 in Supporting Information S1). We maintained each temperature step for 1–2 min to allow the assembly to thermally equilibrate and measure changes in pressure. Before heating to fusion of the starting glass, we started to record a sequence of radiographic images using an exposure time of 0.02–0.05 s. We then heated the assembly rapidly at several hundred degrees per minute to temperatures above the albite melting curve to fully melt the glass and allow the spheres to fall. We attempted to collect an energy dispersive X-ray spectrum from the pressure marker immediately following the fall of the sphere (s). However, we were unable to collect a pattern with clearly resolvable peaks corresponding to the marker. The degradation in the pattern is likely due to rapid recrystallization of MgO at the peak temperature. We estimated the pressure at the peak temperature using the pressure-temperature trends from our experiments (Figure S3 in Supporting Information S1) and previous work using similar assemblies (Edwards, 2019; Leinenweber et al., 2012). We immediately quenched the experiment after scanning the pressure marker. We note the quenched products show a glassy texture with no obvious signs of significant crystallization (Figure S6 in Supporting Information S1).

4. Results

To measure the terminal velocity of the spheres as required by Stokes' Law (Equation 1), we used a MATLAB code to track the spheres through time in the video images. The change in position of the spheres with each frame yields the falling or sinking distance. We note that the spheres quickly developed linear falling-distance versus time profiles as they began to sink. The distance-time profiles display sharp inflections as the spheres approach the end of their falls, that is, the bottom of the capsules, during landing. After the spheres landed, the falling distance stopped changing with time (Figure 2).

To identify the terminal velocities (U_∞), we calculated the sphere settling velocities (U) from the changes in position from starting locations over time. We find that the sphere velocities show three distinct trends during each experiment. The first trend displays increasing velocities (Figure 2) which is characteristic of an acceleration stage of the sphere (Figure 1). The second trend in each experiment shows a constant velocity versus the falling distance or time. The plateau in stage two yields the terminal velocity of the spheres as the buoyancy force and viscous drag force have balanced, that is, Stokes' Law is achieved (Figure 1). We note that these first two stages of U correspond to the linear distance-time profiles (Figure 2). Yet the U_∞ plateau is a fraction of the total linear trend. This indicates that the linear trend alone may not adequately capture the terminal velocity required by Stokes' Law. We also note that the U_∞ from our experiments scale with the sphere sizes (Table 5). This is consistent with an increasing sinking force, that is, negative buoyancy, with volume of the sphere (Section 2.1). Finally, the third stage of the sphere fall shows a sharp decrease in U with distance (Figure 2). We note an inflection in this third stage which suggests the sphere may be slowing as it approaches the bottom of the capsule.

5. Discussion

5.1. The Roles of End Effect Drag and Thermal Gradients

We sought to compare the influence of the wall and end corrections on the estimated viscosity of our aluminosilicate melts. Yet, there is the notable ambiguity in the application of the end correction scheme (Section 2.2.3). The greatest ambiguity lies in the height to apply in the end correction, that is, the total height of the container, H_c, or the distance between the sphere and bottom of the capsule, z. The description of the latter, z, suggests it varies as the sphere sinks. Hence we first sought to clarify the application of the end correction alone before comparing it to other schemes.

To better understand how drag from the capsule end(s) affects Stokes' Law, we evaluated the settling velocities of spheres in our experiments. We note in our experiments that the spheres slowed dramatically toward the ends of their falls (Figure 2). The slowing may suggest that the drag increases as the sphere begins to land, that is, the end effect varies with the distance between the sphere and bottom of capsule (Figure 1). Hence, Equations 4–8 may be best described using the variable z term. Yet we note that some high-pressure work has also suggested that thermal gradients in the chamber could slow the descent of the sphere by increasing the melt viscosity (Reid et al., 2003; Rubie et al., 1993). For simplicity, we refer to this as the thermal gradient effect.

To distinguish the effects of drag and a thermal gradient acting on the sphere velocities, we consider a case in which a 100 μm diameter Re sphere falls from top to bottom of the capsule in our typical assembly (Figure 3). We modeled a thermal gradient along the axis of the capsule and targeted 1973 K at the center (Hernlund et al., 2006), after our experiments. We predict less than 30 K variation from top to bottom of the capsule (Figure 3, inset). We modeled the viscosity of an albitic melt at ambient pressure across this thermal profile (Giordano et al., 2008). We predicted the velocities of the sphere at any point along the center axis using the uncorrected Stokes' Law, that is, Equation 1. We note Equation 1 assumes that the sphere has attained terminal velocity, that is, the viscous and gravitational forces are balanced (Figure 1). This assumption prevents us from examining the acceleration or deceleration of the sphere before and after reaching terminal velocity, respectively. Hence, Equation 1 will allow us to gauge the mechanism that slows the spheres, that is, end effect drag or increasing viscosity by thermal gradients, after terminal velocity is achieved.

The predicted sphere velocities decrease slightly toward the top and bottom of the capsule where temperatures are cooler (Figure 3). We note that this decrease due to temperature is small, that is, $\lesssim$7% of the maximum velocity. As a result, the predicted distance versus time profile is nearly linear toward the bottom of the capsule (Figure 3). In contrast, our experiments display sharp, nonlinear increases in the settling time as the spheres land. This translates to sharp decreases in the sphere velocity close to landing (Figure 2). Hence, thermal gradients in our

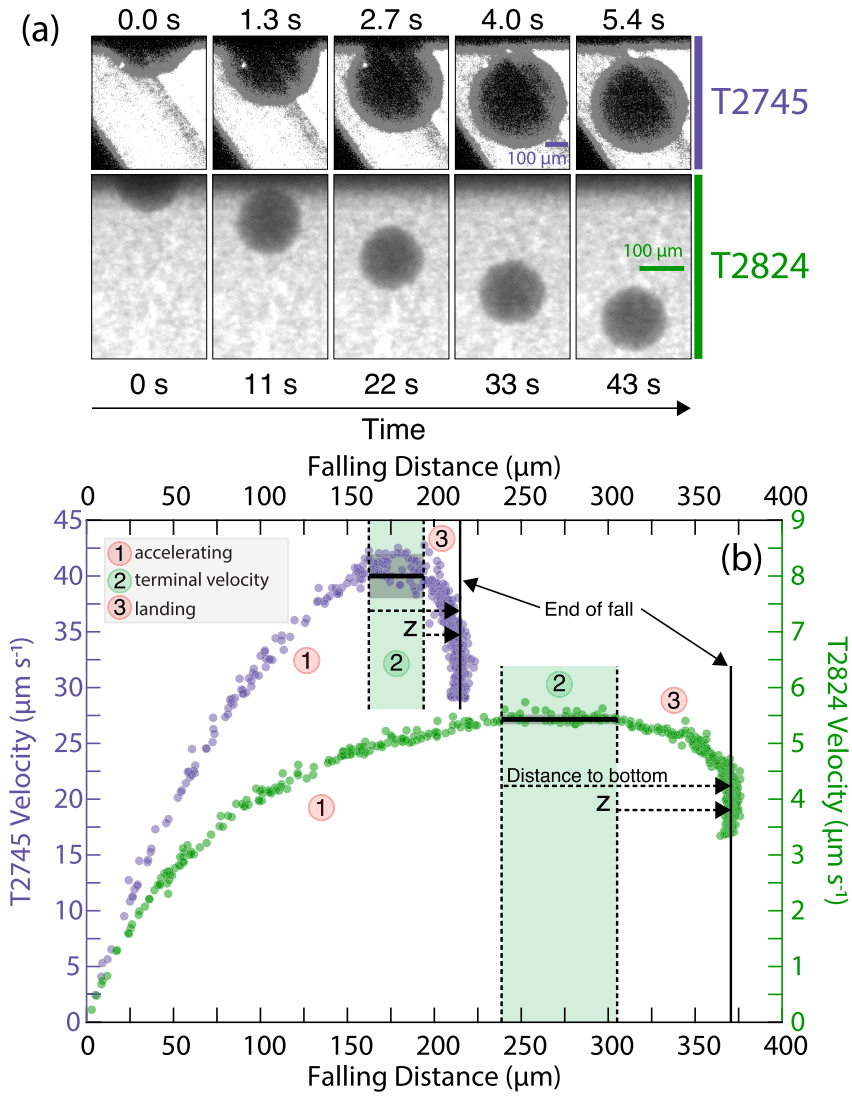

Figure 2. (a) Sequential snapshots of falling rhenium spheres in experiments T2745 (top) and T2824 (bottom). Numbers give the time for each snapshot. Scalebars indicate 100 µm and are color-coded by experiment. (b) Velocity profiles of the spheres. Results for each experiment are plotted on separate vertical axes clarity. The results and corresponding axes are color-coded as in (a). There are three recognized stages for a falling sphere which correspond to (1) acceleration at the beginning of the fall, (2) constant velocity as the buoyancy and viscous drag forces balance, and (3) landing of the sphere (Figure 1). A faded green background highlights stage 2 for clarity. The terminal velocities of the spheres are identified in stage 2 by the plateau. The terminal velocities are calculated by linear regression of the falling distance versus time data and are indicated by bold black lines. The value z gives the distance between the terminal velocity and the bottom of the capsule and is shown by dashed arrows.

assembly may not be strong enough to account for the slowing of the spheres alone. Instead, additional drag from the end of the capsule may be needed to slow the spheres.

Assuming end effect drag is independent of the sphere position, that is, $z = H_C$, we predict that the sphere velocities will be ~3% lower across the entire capsule (Figure 3). We find that the constant drag effect does not significantly alter the trends predicted by the thermal gradient. This suggests that a constant end effect is also not sufficient to describe the slowing of the spheres observed in our experiments (Figure 2).

We find that the slowing of the spheres is well described by drag which varies with distance between the sphere and bottom of capsule. Increasing end effect drag toward the bottom of the capsule strongly decreases the predicted sphere velocities (Figure 3). The result is a nonlinear distance versus time profile in which the settling times

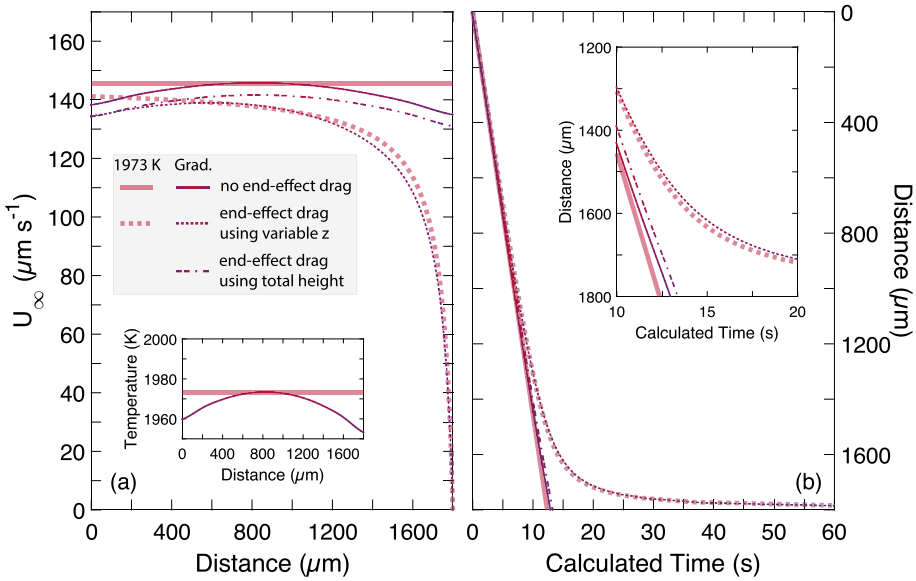

Figure 3. (a) Predicted terminal velocities (U_∞) of a 100 μm rhenium sphere falling in albitic melt versus falling distance. The inset shows a thermal gradient predicted for the vertical axis of the sample chamber in our typical experiment assembly (Hernlund et al., 2006). Melt viscosity is calculated at ambient pressure for a 1973 K isotherm and along the predicted thermal gradient (Giordano et al., 2008). The solid lines show the terminal velocity of the sphere calculated using the uncorrected Stokes' Law (Equation 1), dashed-dotted lines show the U_∞ calculated when applying the end drag effect (Equation 4) (Lorentz, 1907) and assuming z equals the total height of the container (H_c), and the dashed lines show the results from Equation 4 when using a variable z that decreases toward the bottom of the capsule. Thick, faded solid and dashed lines illustrate the results from Equations 1 and 4, respectively, along the isotherm. Panel (b) shows the predicted distance over time profiles from the calculated U_∞ trends. The inset is an expanded view. All lines are color-coded to the temperature gradient shown in the panel (a) inset.

sharply increase as the sphere lands, in good agreement with our experiments (Figure 2). A thermal gradient helps to further slow the sphere with the variable end effect drag. Though we note that comparison to velocities predicted along an isothermal profile shows that the contribution from the thermal gradient is minor for our assembly (Figure 3). We therefore find that the slowing effect is likely dominated by increasing end drag during the fall of the spheres in our experiments. This suggests some minimum height in the sample chamber is needed to ensure the terminal velocity of the sphere is not overshadowed by end effect drag. The chamber height would be dependent on the size of the sphere and experimental device.

5.2. Comparison of Wall and End Corrections

With a better understanding of the end effect, we can now examine the influence of the common correction schemes on Stokes' Law. We calculated the viscosity of our experiments using the uncorrected Stokes' Law, wall and end effect schemes separately and combined (Table 5; Figure 4). To note, we chose Equation 4 (Lorentz, 1907) to evaluate the magnitude of the end correction scheme and used a variable z distance. We measured the z distance as the height at which the sphere achieved terminal velocity, U_∞, above the end of its fall (Figure 2). Notably, the graphite sample capsule could not be easily distinguished from the surrounding ceramics of our multi-anvil assembly due to the relatively low X-ray absorption of these materials. This means that the bottom of the capsule could not be observed directly during the experiment. In cases such as our experiments, the z distance may be most easily identified by observing the sphere landing, that is, where the falling distance stopped changing with time (Figure 2).

The effect of each correction scheme generally increases with d/D (Table 5; Figure 4). Experiment T2824 with $d/D \sim 0.1$, shows nearly a 2-fold change between η_R and η_{WE}. In comparison, experiment T2745 shows a 16-fold change in the calculated viscosity due to a larger d/D of 0.3 (Figure 4). The strongest correction effect is given by combining the wall and end effect schemes (Figure 4). When considered separately, the wall and end effect schemes have variable influence on the calculated viscosity. The wall effect correction directly increases with d/D such that the difference between η_W and η_R is greater for T2745 than T2824 (Table 5; Figure 4). The end effect

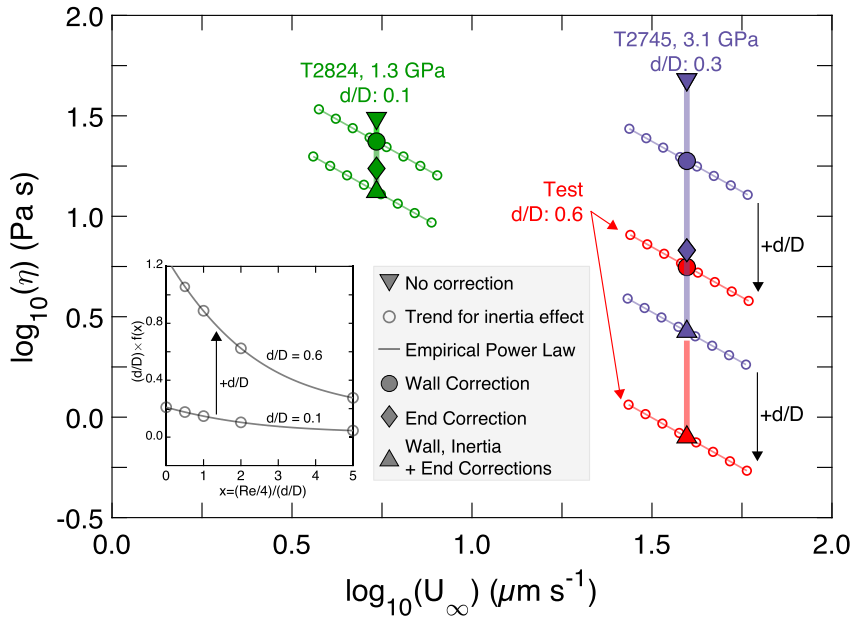

Figure 4. Relationship between the melt viscosity (η) and the terminal velocity of the sphere (U_∞) using Stokes' Law and its various corrections (solid markers). Open circles show numerically calculated trends for Stokes' Law corrected for wall and inertial effects. Thin colored lines show an empirical power law fit to the open circles to determine the viscosity of the experiment. Thick vertical lines connect the upper and lower limits of viscosity. The *d*/*D* provides the ratio of the sphere to capsule diameter. Experiments T2745 and T2824 are shown by purple and green symbols, respectively. The red symbols show a test case in which *d*/*D* for T2745 is assumed to be 0.6. For reference, the inset shows the correction function for inertia of the falling sphere. Open markers are taken from reported values (Brizard et al., 2005; Faxén, 1922) (Table S2 in Supporting Information S1). The gray lines show an empirical third-order polynomial function to interpolate between values.

correction increases with decreasing distance between the sphere and bottom of the capsule (Figure 3). We may gauge the magnitude of the end correction by the number of sphere-diameters for the sphere to fall, that is, $2z/d$ (Tanner, 1963). Experiment T2745 shows an average $2z/d \sim 0.2$ while experiment T2824 shows $2z/d \sim 1.4$ (Table 5). In other words, the sphere in T2745 could only fall at terminal velocity one-fifth of its diameter before landing. In contrast, the sphere in T2824 fell more than one diameter length before landing. Hence, the change between η_E and η_R for T2745 is nearly four-times greater than in T2824 (Figure 4).

We also recast the settling distance for each experiment as $2z/d$ to evaluate changes in the sphere velocities (Figure S7 in Supporting Information S1). We note that experiment T2824 maintains terminal velocity for roughly one diameter-length prior to landing. In contrast, the terminal velocity for T2745 is maintained for less than a quarter of the diameter-length. This figure suggests that the terminal velocity we observe in Figure 2 for T2745 is perhaps not robust. Furthermore, the terminal velocity of T2745 is achieved very close to the bottom of the capsule before landing. This qualitatively suggests that the terminal velocity of T2745 may be more subject to the end drag effects than T2824. The velocity versus $2z/d$ relationship highlights that in experiments such as T2745, very careful consideration of the correction scheme may be needed.

5.3. A Method to Examine Inertia of the Sphere

We also consider the importance of drag due to the inertia of the falling sphere on the calculated melt viscosity. The melt viscosity is relatively simple to be corrected analytically when the inertia term is not considered. The inertia term is challenging to analytically or numerically solve because it is dependent on the Reynolds number, that is, $Re_n = \rho_S U_\infty d/\eta$, and a correction function of Re_n, that is, $f\left(\frac{Re_n/4}{d/D}\right)$, both of which contain the terminal velocity of the sphere (U_∞) and the unknown viscosity of the melt (η) (Brizard et al., 2005; Faxén, 1922). We find that the inertia correction may be readily applied in Stokes' Law when using a semi-graphical approach (Figure 4). We generated a trend in sphere terminal velocities using an arbitrary range of viscosity values input into Equation 3. We find that an empirical power law describes the artificial trends well, that is, Equation 3 can be well

approximated by a power function. We solved the empirical expression analytically to determine the true viscosity of the melt in each experiment.

We find that drag due to inertia of the falling sphere is negligibly small for our experiments. The graphical trends including the inertia scheme overlap entirely with counterpart calculations that do not include this effect (Figure 4). We calculate the Re_n for experiments T2745 and T2848 to be $<10^{-3}$. We note, however, that the inertia term increases with the d/D ratio (Figure 4 inset). Hence drag due to inertia may become more important for large d/D in low viscosity—high sphere-falling-velocity experiments. Such conditions may be relevant for depolymerized silicate melts (Cochain et al., 2017; Spice et al., 2015; Xie et al., 2020, 2021), molten metals (Dobson et al., 2000; LeBlanc & Secco, 1996; Rutter, Secco, Liu, et al., 2002; Rutter, Secco, Uchida, et al., 2002; Terasaki et al., 2001, 2002; Urakawa et al., 2001; Zhu et al., 2022), or volatile-rich fluids (Abramson, 2007, 2009; Abramson & West-Foyle, 2008; Audétat & Keppler, 2004; King et al., 1992).

5.4. Uncertainties in Schemes of Stokes' Law

The large spread in the calculated viscosities at even low d/D indicates poor agreement among the schemes used to account for drag acting on Stokes' Law (Figure 4). However, we note that these calculations give mean values which do not consider the uncertainties in the measurements. Considering the uncertainties may show statistical overlap and thus agreement in the viscosities. Previous work estimated ≤20% error by analytical propagation for the wall scheme in dacitic melt viscosities (Tinker et al., 2004). For combined wall and end corrections, ≤6% error was estimated by Monte Carlo simulations for peridotitic melt viscosities (Xie et al., 2020, 2021). We find that the wall correction in our experiments adjusts the viscosity by ≥24% at even small $d/D \sim 0.11$ (Table 5). This difference in η_W and η_R already exceeds the uncertainty from analytical error propagation. Hence, the uncertainty in the calculated viscosities must be larger than previously considered if the correction schemes are to statistically agree.

To better understand the uncertainties in our Stokes' Law calculations, we performed Monte Carlo simulations in which we randomly varied the measured parameters (Figure 5). We generated 10^5 random points for each parameter assuming normal distributions (Xie et al., 2020, 2021). We also randomly varied equation of state parameters for Re (Ono, 2022) and albitic melts (Figure S3 in Supporting Information S1) in the Monte Carlo simulations (Table 5). We note that the z distance decreases linearly while a sphere falls under terminal velocity (Figure 2). Therefore, we also considered the uncertainty when values of z are uniformly distributed between the minimum and maximum z (Figure S8 in Supporting Information S1).

Our Monte Carlo simulations suggest ≤4% error in the uncorrected Stokes' Law calculations, that is, η_R, for our experiments (Table 5; Figure 5). Applying the schemes for the wall and/or inertia effects, or η_W and η_{WI}, does not significantly increase the uncertainty of the calculated viscosities (Figure 5). We find that applying the end effect correction alone, that is, η_E, increases the uncertainty to 10% for T2824 and 24% for T2745, that is, $2z/d$ of 1.4 and 0.2, respectively. Combining the wall and end effect corrections, or η_{WE} and η_{WIE}, yields a comparable uncertainty to the end effect correction alone (Table 5; Figure 5). This indicates that the uncertainty in the end effect dominates the combined correction scheme, that is, Equations 7 and 8. Critically, we note that the uncertainty in our calculations only rivals that predicted from error propagation, that is, 20%, when the drag effect schemes are combined for a large d/D or small $2z/d$.

Probability distributions predicted from our Monte Carlo simulations show that η_R, η_W, and η_E are separated by more than ±95% confidence (Figure 5). Only the η_{WE} and η_E overlap at this degree of confidence for our experiments. This indicates that correction schemes largely yield statistically distinct values of viscosity. However, we note that the calculated η converges with decreasing d/D (Figure 5). At $d/D \sim 0.1$, we find that the η_W and η_E may slightly overlap at ±99% confidence. This indicates that $d/D < 0.1$ may yield better statistical agreement among the various correction schemes for Stokes' Law.

We note that increasing d/D has a dramatic effect on the range in calculated viscosities. To gauge the full influence of a large d/D on η, we predicted η for an extreme $d/D \sim 0.6$ (Figures 4 and 5). This d/D is greater than previously used by high-pressure experiments (Tables 1–4; Table S1). For this test case, we assume other measured parameters after experiment T2745 (Table 5). We find that the large d/D predicts a range in possible η that extends nearly two orders of magnitude (Figure 4). The range in η is produced by decreasing η_W and η_{WE}. We note that, despite the very large d/D, there appears to be good agreement between η_E and the test η_W (Figure 5). As

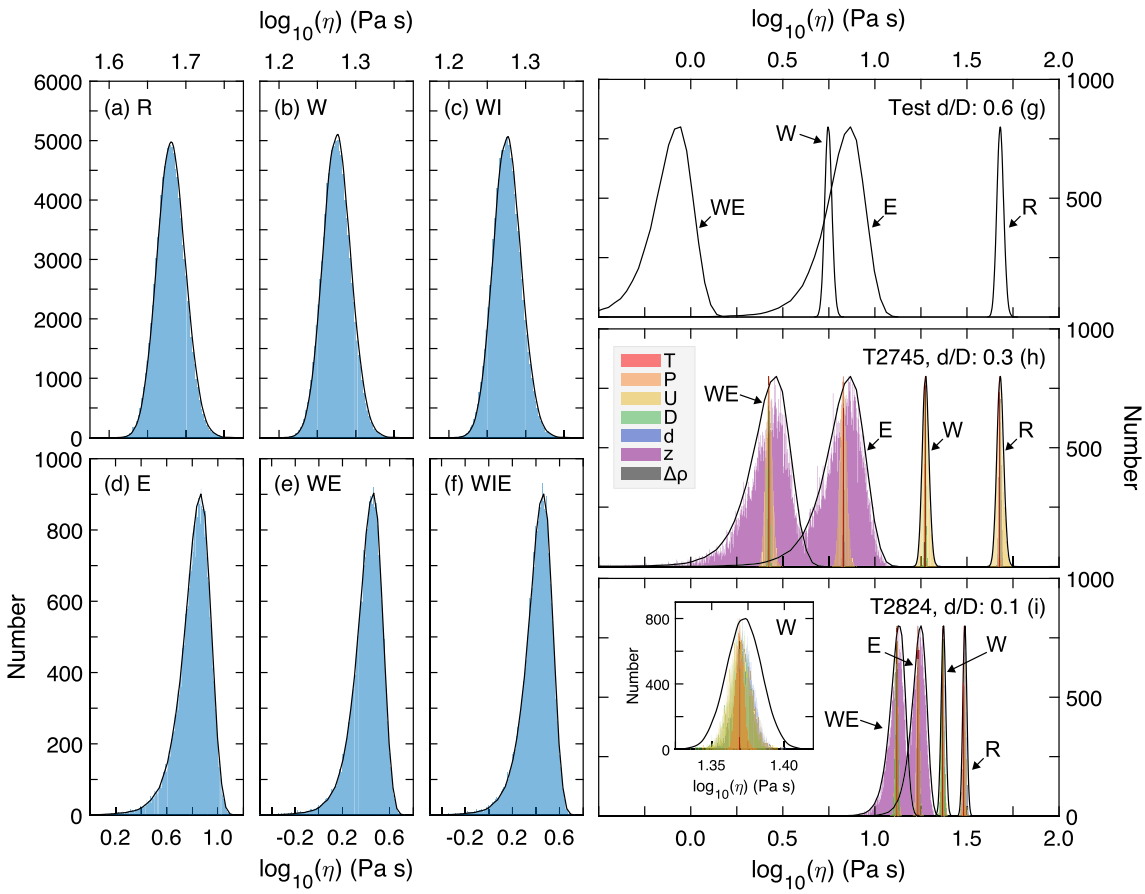

Figure 5. Calculated viscosities from Monte Carlo simulations. Panels (a)–(f) show results for experiment T2745. Blue histograms show results predicted from 10^5 randomized parameters. Bold lines show probability distributions for the results. The R indicates the uncorrected viscosity while W, E, and I indicate the corrections for drag effects due to walls, capsule end and inertia of the falling sphere, respectively. Panels (g)–(h) partial uncertainty analyses in which one parameter is randomly varied 10^4 times. Colored histograms show results for each parameter and are normalized for clarity. Solid lines show bulk probability distributions as done in (a)–(f). Panels (h) and (i) show results for experiments T2745 and T2824, respectively. The *d*/*D* are indicated in each panel. Panel (g) shows a test case in which *d*/*D* is assumed to be 0.6 for T2745.

η_E is directly influenced by $2z/d$ rather than d/D, it provides a cross-comparison for the exaggerated η_W. However, the increased d/D also separates η_E and η_{WE} such that they no longer overlap at ±95 or 99% confidence. Hence, experiments that rely on a large d/D also require very careful choice in the correction scheme for Stokes' Law.

In summary, the experiment results from T2824 show obvious improvement over those from T2745. When using the wall correction alone, the dominant control on this improvement is the lowered d/D in T2824 (Table 5). When using the end correction scheme, the increased $2z/d$ in T2824 also lowers the relative difference in calculated values for η_R and η_E. The common component to these parameters in each correction scheme is the sphere diameter, d. We note some previous experiments relied on very small capsules to achieve extreme pressures relevant to the lower mantle (Xie et al., 2020, 2021). To a first order, it may seem that the simplest method to lowering corrections for Stokes' Law is to use the smallest spheres possible. However, we also note that visibility of the sphere must be maintained in X-ray radiography which limits how small a sphere may be. Large corrections may therefore be unavoidable in certain experiments. In such cases, careful examination or cross-comparisons of the correction schemes may be necessary.

5.5. Controls on Uncertainties in Stokes' Law

The bulk uncertainty we predict from our Monte Carlo simulations for the combined wall and end effect schemes is four times larger than predicted by previous Monte Carlo simulations (Xie et al., 2020, 2021). To note, the previous work also used $d/D \leq 0.3$ as in our experiments (Table 2). We suspect the difference in our error

estimations is due to consideration of the capsule diameter and variable z distance in our study as opposed to the previous work. To better understand the sensitivity of Stokes' Law to the input parameters, we examined the effect of each parameter by randomly varying one measurement 10^4 times while holding the other parameters constant (Figure 5).

We find that the terminal velocity (U_∞) and sphere diameter control the uncertainties for η_R. By accounting for drag due to the capsule walls, we find that the error in η_W shows relatively equal contributions from uncertainties in d, D and U_∞. The small error in η_W, that is, $\leq$4%, is comparable to previous estimates for the combined wall and end schemes, that is, error in η_{WE} is $\leq$6% (Xie et al., 2020, 2021). Hence the uncertainty in the capsule diameter from our experiments is not responsible for the increase in error. Yet this small influence of D on the uncertainty of the calculation is surprising given its key role in the wall correction scheme, that is, Equation 2. We hence further tested the control of D on the uncertainty in viscosity by artificially increasing the uncertainty in D by 5%. The increase in error of D results in a comparable change to the uncertainty in η_W. We also find that D becomes the dominant control on the uncertainty of the calculation as its uncertainty increases. Hence, high precision on the sphere and capsule diameters will limit the control of d/D on the uncertainty of the calculated viscosity. This is a critical point as the capsule diameter can dramatically change due to variable deformation with compression depending on the sample and force load. For instance, sintered glass cores with low porosity may deform less than compacted glass powders. Indeed, our own experiments using packed glass powder showed $\leq$30% decrease in the capsule diameters during compression (Table 5). However, melting may also allow rapid deformation to occur due to volume change from the glass to melt transition. Such an effect is independent of the form of the starting glass. Ultimately, it is very important to measure the d/D before and after an experiment. Assuming little to no change in the initial diameter of the capsule may not accurately capture the drag effects acting on the sphere.

To further identify the difference between our uncertainty calculations and previous work, we evaluated the influence of the z distance on η. We find that uncertainty in the z distance contributes nearly the total uncertainty for η_E and η_{WE} in our experiments (Figure 5). The result is a four-fold increase in the total error of the calculation (Table 5). We also note that if z follows a uniform distribution, that is, decreases linearly during the fall time, the resulting distribution of η_E and η_{WE} becomes more strongly skewed (Figure S8 in Supporting Information S1). Hence, the z parameter primarily accounts for the difference in our and previous work (Xie et al., 2020, 2021). We conclude that z should be very carefully constrained when applying the end effect correction scheme.

Notably, previous work typically reported only container heights, that is, H_C, instead of variable z values. This may be applicable to Equation 5 which considered the total height of the capsule container for the end effect drag (Bacon, 1936; Kingery, 1959; Ladenburg, 1907). However, our work suggests that the end effect may be more accurately captured by a variable z (Figure 3). Hence, we consider H_C to be the maximum possible z for the end correction scheme, that is, z_{H_c} (Tables 1–4; Table S1). As a result, our work explores the influence of the smallest z values, and hence $2z/d$, in high-pressure viscometry on the end effect correction schemes. To identify the lower limit of z to minimize the influence of the end correction scheme on η, we extend our analyses to the larger z_{H_c} values from previous work. We sampled three scenarios which used different capsule heights and diameters with different sphere sizes, that is, different d/D and $2z/d$ ratios (Figure 6). We conducted additional Monte Carlo simulations using 10^6 randomized parameters of reported data and/or inferred geometries from these scenarios (Tables 1–4; Table S1).

We find that the viscosity corrected for end effects (η_E or η_{WE}) becomes statistically indistinguishable from the uncorrected viscosity (η_R) when $2z/d$ increases above ten (Figure 6). The separation in calculated viscosities is also dependent on the uncertainties in previous experimental parameters. For relatively small uncertainties in the calculated viscosity, that is, ~3%, the separation in η_E or η_{WE} and η_R becomes obvious (Figure 6). We also note that increasing $2z/d$ seems to weaken any skewing in the distribution of η, that is, we observe normal distributions of η regardless of the correction scheme. For the simulations, we assumed uniform distributions of z_{H_c} because previous sphere landings were either not observed or reported. From our own experiment results, uniform distributions of z strongly skew the calculations of η (Figure S8 in Supporting Information S1). Clearly the control of the end effect scheme on η weakens remarkably with increasing z values.

We also found that the density contrast ($\Delta\rho$) contributes negligibly to the uncertainties in any form of Stokes' Law (Figure 5). Given the small control of $\Delta\rho$ on the calculated viscosities, we sought to better understand if the density contrast has any control on η. We conducted additional Monte Carlo simulations using results and

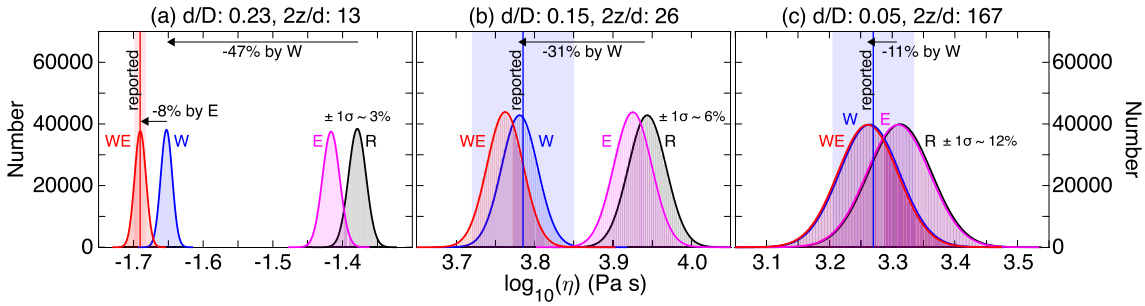

Figure 6. Monte Carlo results corresponding to experiment (a) S3170 from Xie et al. (2020), (b) the 8.5 kbar data from Kushiro (1978), and (c) AOQ3.22 from Schulze et al. (1996). The uncorrected (R) Stokes' Law value is shown in gray histograms. The separate correction schemes for the wall (W) and end (E) effects are shown in blue and pink histograms, respectively. The combined W and E corrections are shown in red. Thick solid lines outlining the histograms are probability distribution functions. Reported values are shown by vertical lines which are color-coded based on the correction scheme used in the previous work. Faded vertical bands show the reported uncertainties in previous work at ±1 standard deviation. Note that z for these cases assumes the maximum total falling distance, that is, the container height or H_c.

parameters from previous work (Kushiro, 1978). As a control, we re-calculated the reported viscosity using the density contrast predicted from equations of state for Pt and albitic melt (Section 3). We propagated the uncertainty in $\Delta\rho$ using the Monte Carlo approach with randomized parameters for the equations of state. We tested the density contrast at 75%, 50%, and 25% of its original magnitude (Figure S9 in Supporting Information S1). We find no obvious differences in the calculated viscosities regardless of the value in $\Delta\rho$, that is, the calculated viscosities are statistically indistinguishable (Figure S9 in Supporting Information S1). This is somewhat surprising as previous work has often argued for a large $\Delta\rho$ to reduce its controls on the uncertainties in the viscosity (e.g., Kushiro, 1978; Tinker et al., 2004). The negligible influence of $\Delta\rho$ may be due to its low uncertainties predicted by the Monte Carlo method, that is, the Monte Carlo simulations predict uncertainties in the sphere and melt densities typically below 1% (e.g., Table 5). We reconducted our Monte Carlo simulations when assuming 10% uncertainty in both the sphere and melt densities. At these larger uncertainties, we find an obvious increase in the uncertainty of viscosities at low $\Delta\rho$ (Figure S9 in Supporting Information S1). The reference $\Delta\rho$, that is, ~19 g cm^{-3}, yields ±13% uncertainty in the calculated viscosities, which is consistent with previous estimates at ±15% (Kushiro, 1978). In contrast, $\Delta\rho$ at 25% of the reference value yields ±21% uncertainty in the calculated viscosities (Figure S9 in Supporting Information S1). These results therefore suggest that a low $\Delta\rho$ may achieve statistically consistent results to a high $\Delta\rho$ when the uncertainties in sphere and melt densities are low. We note that a small $\Delta\rho$ is not typical in high-pressure viscometry as dense, platinum-group metals are often used as spheres (Section 3). Lower values of $\Delta\rho$ may be achieved by using composite spheres of metal and oxides. For instance, early viscometry on Fe-S melts relied on platinum spheres coated in alumina to prevent reaction between the sphere and melt (Secco, 1994). Lower density contrasts in silicate melt studies might therefore also be accomplished by using oxide spheres coated in metal. However, we note that it is technically challenging to produce such spheres. A small $\Delta\rho$ will also lower the sinking force acting on the sphere, which may not be desirable. While our results indicate precision may not be lost with lowering $\Delta\rho$, careful consideration must still be made for future work.

5.6. Choosing the Most Appropriate Scheme

Our calculations emphasize that the choice in correction scheme to Stokes' Law is not a trivial one. The correction schemes produce statistically distinct values of η for $d/D \geq 0.1$ (Figure 5). To identify the most appropriate scheme for high-pressure experiments, we compared our calculations to previous high-pressure work on albitic melts (Figure 7). At 3.1 ± 0.5 GPa, that is, the same pressure as experiment T2745, previous work indicates ~5–15 Pa s using only the wall correction scheme. The range is due to variations in temperature and pressure in the experiments. We calculated 2.9–18.9 Pa s for η_{WE} to η_W, respectively, for T2745. The individual correction schemes show good agreement with previous work (Figure 7). Yet we note that the range in η from the corrections alone spans the same range as the previous measurements from 2.6 to 3.6 GPa. The effect worsens with increasing d/D. Using our test case of $d/D \sim 0.6$, we predict 48 to 0.9 Pa s from η_R to η_{WE}. For comparison, the previous work on albitic melt viscosity shows a general decrease from 16 to 0.3 Pa s between 2 and 7 GPa at ~ 2000 K. Hence, the corrections using a large d/D could account for the entire pressure effect observed in albitic melt (Figure 7). We note that η_W at $d/D \sim 0.6$ is predicted to be 5.6 Pa s which agrees well with previous work at the same pressure,

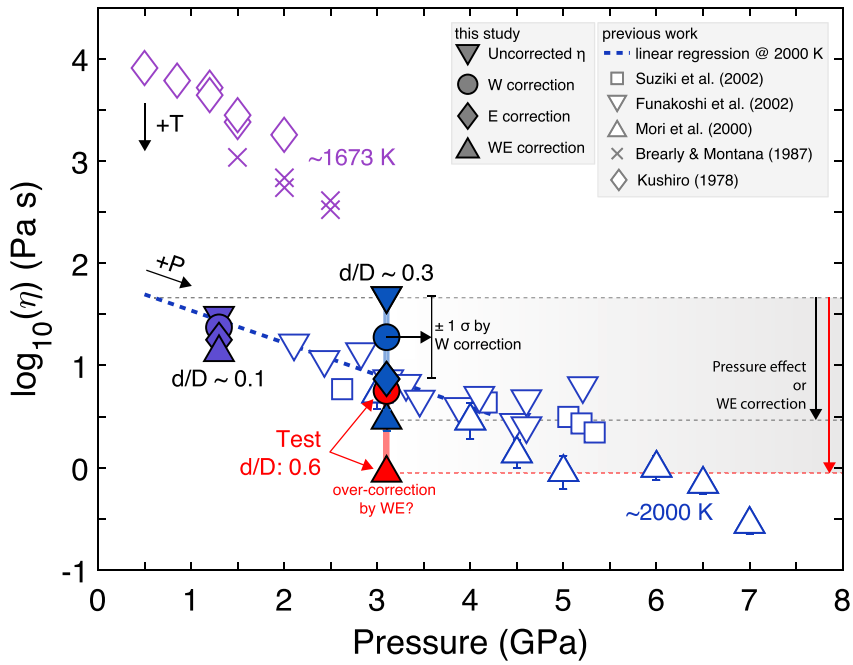

Figure 7. Viscosity (η) of albitic melts as a function of pressure and temperature. Results from this study are shown by solid markers: down-triangles indicate the uncorrected Stokes' Law, circles indicate the η corrected by the wall scheme (W), diamonds by the end scheme (E), and up-triangles by the combined wall and end schemes (WE). The red symbols indicate the test case d/D of 0.6. Hollow symbols and crosses show results from previous experiments (Brearley & Montana, 1989; Funakoshi et al., 2002; Kushiro, 1978; Mori et al., 2000; Suzuki et al., 2002). Error bars indicate ±1 standard deviation of uncertainty. From this work, propagated uncertainties at $\pm 1\sigma$ are smaller than the marker size and are estimated from the Monte Carlo simulations. Uncertainties for previous work are taken from reported values. The dashed blue line highlights the linear trend constrained by previous work at <4.5 GPa. The horizontal, dashed gray and red lines highlight the range of viscosities calculated for our results at ~3 GPa (experiment T2745).

that is, ~3 GPa. Also, η_E is independent of the test d/D and is 7 Pa s. Hence, the separate η_W and η_E may still produce reasonable estimates of the melt viscosity despite the extreme or exaggerated d/D. The cross-comparison of the separate correction schemes is also clearly useful for examining the possible viscosity. Notably, combining the schemes for drag, that is, η_{WE}, accounts for the largest change in η with increasing d/D. This suggests that combining the schemes for drag due to the capsule walls and bottom could severely overcorrect the viscosity (Brizard et al., 2005; Flude & Daborn, 1982; Sutterby, 1973).

If the drag schemes for wall and end effects should be considered separately, which of the two may be most appropriate for high-pressure experiments? We note that η_E shows significantly greater uncertainty than η_W (Figure 5). The probability distribution of η_E is also strongly controlled by whether z follows a normal or uniform distribution (Figure S8 in Supporting Information S1). Our Monte Carlo simulations highlight that the uncertainty in η_E is dominated by the z distance (Figure 5). The uncertainty in η_E inversely scales with $2z/d$ in our experiments. Hence, the end correction may be more precise when $2z/d$ is large, that is, the sphere is small and z is large. We note that measuring z is most accurately done when both the terminal velocity and sphere landing can be observed (Figures 2 and 3). Yet only a fraction of the cell assembly may be viewable using X-ray radiography due to the absorption from the anvils and other components. If the sphere lands out of view, z may not be precisely determined. We also note that previous theoretical and experimental work suggests that the end correction becomes ineffective when $d/D < 0.125$ and the total length of the fall is longer than a couple sphere diameters (Sutterby, 1973). This may place an upper limit to $2z/d$ for which η_E is useful. Therefore, the end effect scheme may be most applicable when the sphere reaches terminal velocity near the bottom of the cell (Brizard et al., 2005) and the landing is viewable. For instance, our experiment T2745 shows excellent agreement between η_E and previous work on albitic melts (Figure 7) despite the very small $2z/d$ at which the terminal velocity occurs (Figure S7 in Supporting Information S1). However, these conditions will also increase the uncertainty in the end correction scheme (Table 5; Figure 5).

In lieu of the end effect scheme, the wall effect scheme may be the most broadly applicable for high-pressure experiments. The diameters of the sphere and capsule can be measured before and after an experiment to precisely determine d/D. However, we note that the accuracy of the wall correction has been contested for silicate melts. Ambient-pressure experiments on synthetic sodium aluminosilicate melt showed that η_W calculated from Stokes' Law was ≥10% lower than measured by rotational viscometry (Kahle et al., 2003). Regardless, no other correction to account for drag from the capsule walls has been proposed. We also note that our calculated values of η_E are smaller than η_W (Table 5; Figure 4). Hence if η_W underestimates the viscosity, η_E must as well. Given the convenience and precision of η_W over η_E, the wall correction may still be the appropriate scheme for most applications of Stokes' Law at high pressure.

Considering that η_W may underestimate the viscosity of silicate melts, we evaluate the magnitude of the possible inaccuracy. At ±95% confidence, our experiments show ≤8% error at $d/D \leq 0.3$ (Table 5). Assuming η_W consistently overcorrects silicate melt viscosity regardless of intensive variable, the error in our results may account for most of the inaccuracy, that is, ≥10% (Kahle et al., 2003). We also note that silicate melt viscosity operates on a logarithmic scale with pressure and temperature. Considering the logarithmic values of melt viscosity lowers the difference in η between Stokes' Law and rotational viscometry to <5% (Kahle et al., 2003). Hence the inaccuracy may not be significant for constraining effects of pressure and temperature on silicate melt viscosity.

To further reduce the inaccuracy of the measurements, we note that the error predicted by our Monte Carlo simulations is overshadowed by the first-order correction for drag (Figure 5). Increasing d/D further exaggerates the correction effect and may result in greater inaccuracies to η_W (Kahle et al., 2003). Hence, the error predicted by Monte Carlo simulations may not capture the realistic uncertainty in Stokes' Law viscometry on silicate melts. Assuming the uncorrected Stokes' Law overestimates the melt viscosity, the true viscosity should lie somewhere between η_R and η_W. To capture this η, we suggest considering the magnitude of the correction as a more realistic uncertainty, that is, $100 \cdot (1 - \eta_W/\eta_R)$. Lowering d/D will also help to reduce the necessary corrections for drag and produce a more accurate measurement on η (Figures 4–7).

To further evaluate the correction schemes for Stokes' Law, we examined their influence on previous viscometry at high-pressures (Tables 1–4; Table S1). To directly compare previous studies, we extracted, recalculated, or estimated previous correction factors across the range of used d/D ratios (Figure 8). The correction factor (C_f) is equal to the corrected viscosity over the raw viscosity, that is, η_C/η_R. The percent change in C_f is given by $100 \cdot (1 - \eta_C/\eta_R)$ and can serve as a proxy for the total uncertainty in the measurements. We estimate C_f using each scheme that accounts for drag acting on Stokes' Law, that is, Equations 1–8.

We find two general trends in C_f versus d/D (Figure 8). The effect of C_f based on the end effect scheme alone weakly increases with d/D and displays jagged forms that are largely independent of d/D. The increase in the effect of C_f is attributed to a shrinking available falling distance as the sphere size increases, that is, decreasing $2z/d$. The large peaks highlight the strong effect of the total falling distance on C_f. Small values of z dramatically increase C_f regardless of sphere size. We find that Equation 4 (Lorentz, 1907) and Equation 5 (Bacon, 1936; Kingery, 1959; Ladenburg, 1907) agree very well. We find that Equation 6 (Maude, 1961) consistently produces a larger correction effect than Equations 4 and 5 (Figure 8). Since Equation 6 was formulated considering two falling spheres, the larger effect of C_f from Equation 6 is likely due to additional drag for a two-body system. Equation 6 may not be appropriate if only one sphere is used in an experiment.

The wall correction produces a continuous increase in the change by C_f and forms a baseline for the second trend (Figure 8). Combining the end and wall schemes adds the jagged form of the end correction. The result is that the combined schemes significantly increase the effect of C_f. If the wall correction alone overcorrects the melt viscosity (Kahle et al., 2003), these results highlight that the combined schemes for drag may even more so overcorrect the viscosity. The overcorrection is likely worsened for cases where z is small and/or if the end correction becomes unreliable with decreasing d/D (Sutterby, 1973).

5.7. The Influence of High-Pressure Devices on Stokes' Law

Molten and vaporous geofluids are expected to occur throughout Earth and other planetary bodies. Because these geofluids are highly mobile compared to solid rock, the geofluids promote relatively rapid geologic processes such as magmatism and volcanism. The viscosity of geofluids strongly influences the mobility of the geofluid and

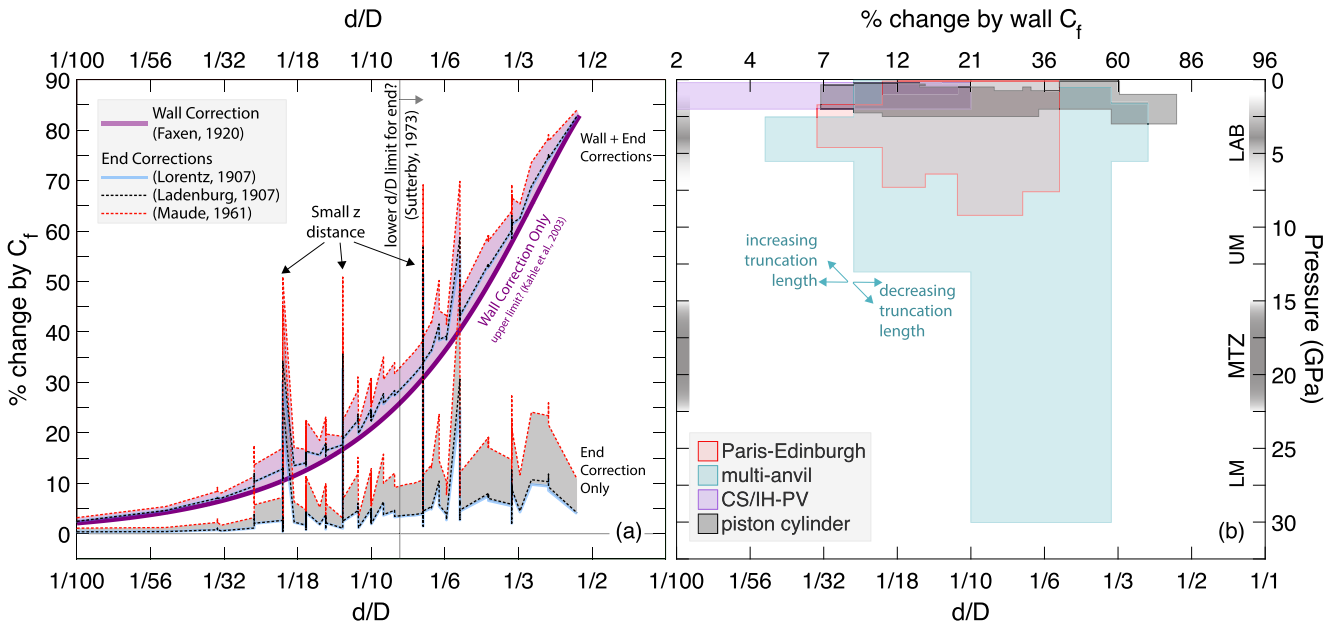

Figure 8. (a) Percent change in calculated viscosity by various correction terms for falling sphere viscometry at high-pressures. The % change by C_f equals $100 \cdot (1 - \eta_C/\eta_R)$, where $C_f = \eta_C/\eta_R$ or the ratio of corrected and uncorrected viscosities, respectively. The blue faded lines, black and red dashed lines are calculated using Equations 4–6, respectively (Bacon, 1936; Kingery, 1959; Ladenburg, 1907; Lorentz, 1907; Maude, 1961). The purple faded line is calculated using Equation 2 (Faxén, 1922). The faded gray and purple areas highlight the end terms when isolated or combined with the wall term, respectively. For reference, thin solid lines indicate where $C_f = 1$, that is, 0% change, and the possible lower d/D limit of the end correction (Sutterby, 1973). (b) Relationship of explored pressures and estimated d/D from previous work color-coded by experimental device. For reference, the upper horizontal axis shows the percent change to the calculated viscosity using the wall effect term (Faxén, 1922), that is, $C_f = \eta_W/\eta_R$.For panels (a) and (b), data is taken from the compilation in this study (Tables 1–4; Table S1).

hence their precise role(s) in planetary interiors. Critically, geofluids span an enormous range of chemistry from volatile-rich fluids to molten silicates and metals. The geofluids also persist across an equally large range of pressure and temperature conditions relevant to the crust, mantle, and core.

A wide variety of devices have been developed which can explore the viscosity of geofluids at conditions relevant to the interior of planets (Table S1). These devices include cold-seal or internally heated pressure vessels (CS/IH-PV), piston cylinder and multi-anvil presses, and Paris-Edinburgh devices. Notably, each device is carefully designed to generate specific pressures and temperatures for regions of interest in the planetary interior, that is, the crust, mantle, or core. The fine tuning of each device results in unique geometries which dictate the capsule size to contain a geofluid. These unique geometries will impose specific drag effects on spheres in Stokes' Law viscometry experiments. Hence, it is important to understand the uncertainties that are inherent for each high-pressure device when targeting certain pressures and temperatures for the planet interior.

To gauge the influence of a device on the uncertainties in Stokes' Law, we considered the relationship between explored pressures and d/D ratios for each high-pressure device (Figure 8). We considered the correction to viscosity when accounting only for the wall effects. We note that the end correction scheme may yield greater uncertainties especially when combined with the wall correction scheme. We also note that our evaluation does not consider if inertia due to the sphere is significant for low-viscosity and high-settling-velocity experiments.

We find that CS/IH-PV devices used some of the smallest d/D which led to the smallest uncertainties in the calculated viscosities for previous high-pressure work (Figure 8). This makes the CS/IH-PV devices ideal for limiting corrections to Stokes' Law. However, the CS/IH-PV are also limited to low pressures <2.5 GPa, that is, lithospheric conditions. Viscometry has also been used in piston cylinders to explore similar pressures but with larger d/D, that is, uncertainties up to 82%. We note that the largest d/D used by piston cylinders are from classic works which pioneered modern falling sphere viscometry at high pressures (Kushiro, 1978; Kushiro et al., 1976; Shaw, 1963). More recent work since the late 1980's has used smaller d/D in piston cylinders with uncertainties <40% (Table 1). Although the pressure range is relatively low, an advantage to the piston cylinder is that it may be

combined with a centrifuge to explore highly viscous geofluids at realistic temperatures for the crust and mantle (Ardia et al., 2008).

Higher pressures relevant for the upper mantle, that is, >3 GPa, have been explored in Paris-Edinburgh devices in the last decade or so. Paris-Edinburgh experiments frequently use $d/D < 0.2$ and hence also maintain <40% uncertainties (Figure 8). Melt viscosities at even greater pressures relevant for the upper to lower mantle have been explored in multi-anvil devices. We note that multi-anvil devices have relied on some of the smallest and largest d/D in high-pressure experiments (Figure 8). The range in d/D is due to the size of a multi-anvil pressure medium. The size of the medium depends on the face edge length and anvil truncation edge length to generate pressure (Leinenweber et al., 2012). As a result, the d/D and uncertainty in multi-anvil experiments depends on the target pressure. For instance, viscosities of ultramafic melts at very high pressures <30 GPa have been explored at the expense of increasing corrections to Stokes' Law (Xie et al., 2020, 2021). Yet, multi-anvil devices have also been used to explore low pressures similar to CS/IH-PV and piston cylinders, allowing lower d/D (Figure 8).

An advantage to Paris-Edinburgh and multi-anvil presses is that they are often combined with real-time X-ray radiography. The real-time videos allow accurate determination of terminal velocities which can significantly lower the uncertainty in the calculated viscosity (Funakoshi et al., 2002; Kanzaki et al., 1987). However, we note that the viewing windows for observing the falling sphere shrink significantly with increasing pressure in either device. Paris-Edinburgh experiments also tend to have a short window due to the opposed anvil geometry. This may limit the ability to observe the landing of the sphere and hence identify the z distance. There is therefore a delicate balance between generating the target high pressures and ensuring visibility of the complete sphere fall for the z parameter.

6. Conclusions

In summary, in this study we reviewed various correction schemes to Stokes' Law in measuring viscosity at high-pressures. We evaluated the variations in the viscosity using high-pressure experiments on albitic melts and Monte Carlo simulations. Our analysis indicates that the drag due to end of the capsule may best be explained by a decreasing distance between the sphere and capsule bottom during settling of the sphere. The drag due to inertia of the falling sphere is negligible in viscous melts in which the sphere sinks slowly. However, the drag due to inertia also scales with the sphere-to-capsule diameter ratio (d/D), falling speed of the sphere, and decreasing viscosity of the sample. Monte Carlo simulations indicate that schemes to account for drag acting on Stokes' Law predict statistically distinct viscosities when $d/D \geq 0.1$. When the correction schemes for the effect of the wall and the end of the falling path are combined, it has the largest effect on the calculated viscosity using Stokes' Law. We find these two combined schemes may dramatically overcorrect the calculated viscosity with increasing d/D. The correction scheme due to the end of the falling path alone strongly depends on the distance through which the sphere has descended and associated uncertainties. The falling distance may be most accurately identified if the sphere landing is observed during an experiment. The wall effect correction alone appears most convenient for high-pressure experiments. However, wall correction may become inaccurate with increasing d/D (Kahle et al., 2003). A small d/D is needed to minimize necessary corrections and hence inaccuracy. The primary choice in the scheme to account for drag overshadows the experimental uncertainty in any one scheme. As a result, the uncertainty may be more realistically captured by the change in viscosity due to the correction. Furthermore, the choice in device to generate high pressures should consider the target pressures and temperatures as well as the geometry of the device. The device geometry will place inherent limitations on the correction schemes to Stokes' Law. Hence, balance is required between achieving the target conditions and minimizing uncertainties in the falling sphere viscometry. Notably, we do not observe any obvious relationships between the fluid/melt compositions explored, or their viscosities, and the magnitude of corrections to determine their viscosities. This is because the correction is dependent on the geometry of the high-pressures device used to explore the fluid/melt behavior. As an effort to aid future work, we compiled the previous studies from our review into an Excel-based file (Table S1). Future research may use this data to evaluate and refine efforts from previous experiments based on our findings in this study.

Conflict of Interest

The authors declare no conflicts of interest relevant to this study.

Data Availability Statement

Image sequence stacks, Monte Carlo results, and Table S1 are available in a Zenodo repository (Ashley et al., 2023) https://doi.org/10.5281/zenodo.10278394. The MATLAB code is also available in this repository.

Acknowledgments
A.W.A. acknowledges the Buie, DeVore, and Watkins Fund from the Department of Earth, Ocean and Atmospheric Sciences, FSU. M. M. acknowledges the National Science Foundation Grant (EAR-2246802, and EAR-1753125) for funding this research. M. M. also acknowledges the Global Visitor Fellowship from the Earth and Plants Laboratory, Carnegie Institution for Science, Washington DC. Y.W. acknowledges NSF support via EAR-2246803. Portions of this work were performed at GeoSoilEnviroCARS (The University of Chicago, Sector 13), APS, Argonne National Laboratory. GeoSoilEnviroCARS is supported by the National Science Foundation—Earth Sciences via SEES: Synchrotron Earth and Environmental Science (EAR-2223273). This research used resources of the APS, a U.S. Department of Energy (DOE) Office of Science User Facility, operated for the DOE Office of Science by Argonne National Laboratory under Contract No. DE-AC02-06CH11357. G. M. acknowledges funding received from INSU and the LabEx ClerVolc (contribution number 647). We thank Tim Officer for help in developing the MATLAB code.

References

Abe, Y. (1997). Thermal and chemical evolution of the terrestrial magma ocean. *Physics of the Earth and Planetary Interiors*, *100*(1–4), 27–39. https://doi.org/10.1016/s0031-9201(96)03229-3

Abramson, E. H. (2007). Viscosity of water measured to pressures of 6 GPa and temperatures of 300°C. *Physical Review E - Statistical, Nonlinear and Soft Matter Physics*, *76*(5), 051203. https://doi.org/10.1103/physreve.76.051203

Abramson, E. H. (2009). Viscosity of carbon dioxide measured to a pressure of 8 GPa and temperature of 673 K. *Physical Review*, *80*(2), 021201. https://doi.org/10.1103/physreve.80.021201

Abramson, E. H., & West-Foyle, H. (2008). Viscosity of nitrogen measured to pressures of 7 GPa and temperatures of 573 K. *Physical Review*, *77*(4), 041202. https://doi.org/10.1103/physreve.77.041202

Allwardt, J. R., Stebbins, J. F., Terasaki, H., Du, L. S., Frost, D. J., Withers, A. C., et al. (2007). Effect of structural transitions on properties of high-pressure silicate melts: ^{27}Al NMR, glass densities, and melt viscosities. *American Mineralogist*, *92*(7), 1093–1104. https://doi.org/10.2138/am.2007.2530

Anovitz, L. M., & Blencoe, J. G. (1999). Dry melting of high albite. *American Mineralogist*, *84*(11–12), 1830–1842. https://doi.org/10.2138/am-1999-11-1210

Anzellini, S., Monteseguro, V., Bandiello, E., Dewaele, A., Burakovsky, L., & Errandonea, D. (2019). In situ characterization of the high pressure – High temperature melting curve of platinum. *Scientific Reports*, *9*, 1–10. https://doi.org/10.1038/s41598-019-49676-y

Ardia, P., Giordano, D., & Schmidt, M. W. (2008). A model for the viscosity of rhyolite as a function of H_2O-content and pressure: A calibration based on centrifuge piston cylinder experiments. *Geochimica et Cosmochimica Acta*, *72*(24), 6103–6123. https://doi.org/10.1016/j.gca.2008.08.025

Ashley, A. W., Bajgain, S. K., Mookherjee, M., Xu, M., Yu, T., Wang, Y., et al. (2022). Viscosities of anhydrous and hydrous albitic melts at high pressures. In *AGU Fall Meeting Abstracts, V26B-06*.

Ashley, A. W., Mookherjee, M., Xu, M., Yu, T., Manthilake, G., & Wang, Y. (2023). Viscosity measurements at high pressures: A critical appraisal of corrections to Stokes' Law [Dataset]. *Zenodo*. https://doi.org/10.5281/zenodo.10278394

Audétat, A., & Keppler, H. (2004). Viscosity of fluids in subduction zones. *Science*, *303*(5657), 513–516. https://doi.org/10.1126/science.1092282

Bacon, L. R. (1936). Measurement of absolute viscosity by the falling sphere method. *Journal of the Franklin Institute*, *221*(2), 251–273. https://doi.org/10.1016/s0016-0032(36)90395-2

Bajgain, S. K., Ashley, A. W., Mookherjee, M., Ghosh, D. B., & Karki, B. B. (2022). Insights into magma ocean dynamics from the transport properties of basaltic melt. *Nature Communications*, *13*(1), 7590. https://doi.org/10.1038/s41467-022-35171-y

Bajgain, S. K., & Mookherjee, M. (2020). Structure and properties of albite melt at high pressures. *ACS Earth and Space Chemistry*, *4*, 1–13. https://doi.org/10.1021/acsearthspacechem.9b00187

Baker, D. R., & Vaillancourt, J. (1995). The low viscosities of F + H_2O-bearing granitic melts and implications for melt extraction and transport. *Earth and Planetary Science Letters*, *132*(1–4), 199–211. https://doi.org/10.1016/0012-821x(95)00054-g

Behrens, H., & Schulze, F. (2003). Pressure dependence of melt viscosity in the system $NaAlSi_3O_8$-$CaMgSi_2O_6$. *American Mineralogist*, *88*(8–9), 1351–1363. https://doi.org/10.2138/am-2003-8-919

Belonoshko, A. B., & Rosengren, A. (2012). High-pressure melting curve of platinum from *ab initio* Z method. *Physical Review B: Condensed Matter and Materials Physics*, *85*(17), 1–7. https://doi.org/10.1103/physrevb.85.174104

Bonechi, B., Stagno, V., Kono, Y., Hrubiak, R., Ziberna, L., Andreozzi, G. B., et al. (2022). Experimental measurements of the viscosity and melt structure of alkali basalts at high pressure and temperature. *Scientific Reports*, *12*(1), 2599. https://doi.org/10.1038/s41598-022-06551-7

Boyd, F. R., & England, J. L. (1963). Effect of pressure on the melting of diopside, $CaMgSi_2O_6$, and albite, $NaAlSi_3O_8$, in the range up to 50 kilobars. *Journal of Geophysical Research*, *68*(1), 311–323. https://doi.org/10.1029/jz068i001p00311

Brearley, M., Dickinson, J. E., & Scarfe, C. M. (1986). Pressure dependence of melt viscosities on the join diopside-albite. *Geochimica et Cosmochimica*, *50*(12), 2563–2570. https://doi.org/10.1016/0016-7037(86)90210-3

Brearley, M., & Montana, A. (1989). The effect of CO_2 on the viscosity of silicate liquids at high pressure. *Geochimica et Cosmochimica Acta*, *53*(10), 2609–2616. https://doi.org/10.1016/0016-7037(89)90132-4

Brizard, M., Megharfi, M., Mahé, E., & Verdier, C. (2005). Design of a high precision falling-ball viscometer. *Review of Scientific Instruments*, *76*(2), 025109. https://doi.org/10.1063/1.1851471

Burakovsky, L., Burakovsky, N., Preston, D., & Simak, S. (2018). Systematics of the third-row transition metal melting: The HCP metals rhenium and osmium. *Crystals*, *8*(6), 243. https://doi.org/10.3390/cryst8060243

Bureau, H., & Keppler, H. (1999). Complete miscibility between silicate melts and hydrous fluids in the upper mantle: Experimental evidence and geochemical implications. *Earth and Planetary Science Letters*, *165*(2), 187–196. https://doi.org/10.1016/s0012-821x(98)00266-0

Castro, J. M., & Dingwell, D. B. (2009). Rapid ascent of rhyolitic magma at Chaitén volcano, Chile. *Nature*, *461*(7265), 780–783. https://doi.org/10.1038/nature08458

Cochain, B., Sanloup, C., Leroy, C., & Kono, Y. (2017). Viscosity of mafic magmas at high pressures. *Geophysical Research Letters*, *44*(2), 818–826. https://doi.org/10.1002/2016gl071600

Dickinson, J. E., Scarfe, C. M., & McMillan, P. (1990). Physical properties and structure of $K_2Si_4O_9$ melt quenched from pressures up to 2.4 GPa. *Journal of Geophysical Research*, *95*(B10), 15675–15681. https://doi.org/10.1029/jb095ib10p15675

Dingwell, D. B. (1987). Melt viscosities in the system $NaAlSi_3O_8$-H_2O-F_2O. *Magmatic Processes: Physicochemical Principles*, *1*, 423–433.

Dingwell, D. B. (1995). *Viscosity and anelasticity of melts. Mineral physics and crystallography: A handbook of physical constants* (pp. 209–217). AGU.

Dobson, D. P., Crichton, W. A., Vocadlo, L., Jones, A. P., Wang, Y., Uchida, T., et al. (2000). In situ measurement of viscosity of liquids in the Fe-FeS system at high pressures and temperatures. *American Mineralogist*, *85*(11–12), 1838–1842. https://doi.org/10.2138/am-2000-11-1231

Dobson, D. P., Jones, A. P., Rabe, R., Sekine, T., Kurita, K., Taniguchi, T., et al. (1996). In-situ measurement of viscosity and density of carbonate melts at high pressure. *Earth and Planetary Science Letters*, *143*(1–4), 207–215. https://doi.org/10.1016/0012-821x(96)00139-2

Dunn, T., & Scarfe, C. M. (1986). Variation of the chemical diffusivity of oxygen and viscosity of an andesitic melt with pressure at constant temperature. *Chemical Geology*, *54*(3–4), 203–215. https://doi.org/10.1016/0009-2541(86)90137-3

Dygert, N., Lin, J. F., Marshall, E. W., Kono, Y., & Gardner, J. E. (2017). A Low viscosity lunar magma ocean forms a stratified anorthitic flotation crust with mafic poor and rich units. *Geophysical Research Letters*, *44*(22), 11282–11291. https://doi.org/10.1002/2017GL075703

Edwards, P. M. (2019). *Viscosity of iron-rich silicate melts by falling sphere viscometry at high pressure: Implications for the mobility of pyroxenitic melts in the mantle*. University of California.

Eilon, Z. C., & Abers, G. A. (2017). High seismic attenuation at a mid-ocean ridge reveals the distribution of deep melt. *Science Advances*, *3*(5), e1602829. https://doi.org/10.1126/sciadv.1602829

Elkins-Tanton, L. T. (2012). Magma oceans in the inner solar system. *Annual Review of Earth and Planetary Sciences*, *40*(1), 113–139. https://doi.org/10.1146/annurev-earth-042711-105503

Faxén, H. (1922). Der Widerstand gegen die Bewegung einer starren Kugel in einer zahen Flussigkeit, die zwischen zwei parallelen ebenen Wanden eingeschlossen ist. *Annalen der Physik*, *373*(10), 89–119. https://doi.org/10.1002/andp.19223731003

Fidleris, V., & Whitmore, R. L. (1961). Experimental determination of the wall effect for spheres falling axially in cylindrical vessels. *British Journal of Applied Physics*, *12*(9), 490–494. https://doi.org/10.1088/0508-3443/12/9/311

Flude, M. J. C., & Daborn, J. E. (1982). Viscosity measurement by means of falling spheres compared with capillary viscometry. *Journal of Physics E: Scientific Instruments*, *15*(12), 1313–1321. https://doi.org/10.1088/0022-3735/15/12/013

Francis, A. W. (1933). Wall effect in falling ball method for viscosity. *Journal of Applied Physics*, *4*(11), 403–406. https://doi.org/10.1063/1.1745151

Funakoshi, K., Suzuki, A., & Terasaki, H. (2002). In situ viscosity measurements of albite melt under high pressure. *Journal of Physics: Condensed Matter*, *14*(44), 11343–11347. https://doi.org/10.1088/0953-8984/14/44/479

Gaudio, S. J., Lesher, C. E., Maekawa, H., & Sen, S. (2015). Linking high-pressure structure and density of albite liquid near the glass transition. *Geochimica et Cosmochimica*, *157*, 28–38. https://doi.org/10.1016/j.gca.2015.02.017

Giordano, D., Russell, J. K., Dingwell, D. B., & Tot, F. (2008). Viscosity of magmatic liquids: A model. *Earth and Planetary Science Letters*, *271*(1–4), 123–134. https://doi.org/10.1016/j.epsl.2008.03.038

Hacker, B. R. (2008). H_2O subduction beyond arcs. *Geochemistry, Geophysics, Geosystems*, *9*(3), Q03001. https://doi.org/10.1029/2007gc001707

Hermann, J., Spandler, C., Hack, A. C., & Korsakov, A. V. (2006). Aqueous fluids and hydrous melts in high-pressure and ultra-high-pressure rocks: Implications for element transfer in subduction zones. *Lithos*, *92*(3–4), 399–417. https://doi.org/10.1016/j.lithos.2006.03.055

Hernlund, J., Leinenweber, K., Locke, D., & Tyburczy, J. A. (2006). A numerical model for steady-state temperature distributions in solid-medium high-pressure cell assemblies. *American Mineralogist*, *91*(2–3), 295–305. https://doi.org/10.2138/am.2006.1938

Holtz, F., Roux, J., Ohlhorst, S., Behrens, H., & Schulze, F. (1999). The effects of silica and water on the viscosity of hydrous quartzofeldspathic melts. *American Mineralogist*, *84*(1–2), 27–36. https://doi.org/10.2138/am-1999-1-203

Kahle, A., Winkler, B., & Hennion, B. (2003). Is Faxén's correction function applicable to viscosity measurements of silicate melts with the falling sphere method? *Journal of Non-Newtonian Fluid Mechanics*, *112*(2–3), 203–215. https://doi.org/10.1016/s0377-0257(03)00098-3

Kanzaki, M., Kurita, K., Fujii, T., Kato, T., Shimomura, O., & Akimoto, S. (1987). A new technique to measure the viscosity and density of silicate melts at high pressure. *High-Pressure Research in Mineral Physics*, *39*, 195–200. https://doi.org/10.1029/gm039p0195

Karki, B. B., & Stixrude, L. P. (2010). Viscosity of $MgSiO_3$ liquid at Earth's mantle conditions: Implications for an early magma ocean. *Science*, *328*(5979), 740–742. https://doi.org/10.1126/science.1188327

Kavner, A., & Jeanloz, R. (1998). High-pressure melting curve of platinum. *Journal of Applied Physics*, *83*(12), 7553–7559. https://doi.org/10.1063/1.367520

Kessel, R., Schmidt, M. W., Ulmer, P., & Pettke, T. (2005). Trace element signature of subduction-zone fluids, melts and supercritical liquids at 120-180 km depth. *Nature*, *437*(7059), 724–727. https://doi.org/10.1038/nature03971

Kessel, R., Ulmer, P., Pettke, T., Schmidt, M. W., & Thompson, A. B. (2005). The water-basalt system at 4 to 6 GPa: Phase relations and second critical endpoint in a K-free eclogite at 700 to 1400°C. *Earth and Planetary Science Letters*, *237*(3–4), 873–892. https://doi.org/10.1016/j.epsl.2005.06.018

Key, K., Constable, S., Liu, L., & Pommier, A. (2013). Electrical image of passive mantle upwelling beneath the northern East Pacific Rise. *Nature*, *495*(7442), 499–502. https://doi.org/10.1038/nature11932

King, H. E., Herbolzheimer, E., & Cook, R. L. (1992). The diamond-anvil cell as a high-pressure viscometer. *Journal of Applied Physics*, *71*(5), 2071–2081. https://doi.org/10.1063/1.351157

Kingery, W. D. (1959). *Property measurements at high temperatures: Factors affecting and methods of measuring material properties at temperatures above 1400°C*. Wiley.

Kobsch, A., & Caracas, R. (2020). The critical point and the supercritical state of alkali feldspars: Implications for the behavior of the crust during impacts. *Journal of Geophysical Research: Planets*, *125*(9), e2020JE006412. https://doi.org/10.1029/2020je006412

Kono, Y., Kenney-Benson, C., Hummer, D., Ohfuji, H., Park, C., Shen, G., et al. (2014). Ultralow viscosity of carbonate melts at high pressures. *Nature Communications*, *5*, 1–8. https://doi.org/10.1038/ncomms6091

Kono, Y., Kenney-Benson, C., Park, C., Shen, G., & Wang, Y. (2013). Anomaly in the viscosity of liquid KCl at high pressures. *Physical Review B: Condensed Matter and Materials Physics*, *87*(2), 024302. https://doi.org/10.1103/physrevb.87.024302

Kono, Y., Kenney-Benson, C., Shibazaki, Y., Park, C., Shen, G., & Wang, Y. (2015). High-pressure viscosity of liquid Fe and FeS revisited by falling sphere viscometry using ultrafast X-ray imaging. *Physics of the Earth and Planetary Interiors*, *241*, 57–64. https://doi.org/10.1016/j.pepi.2015.02.006

Kress, V. C., Williams, Q., & Carmichael, I. S. E. (1988). Ultrasonic investigation of melts in the system Na_2O-Al_2O_3-SiO_2. *Geochimica et Cosmochimica Acta*, *52*(2), 283–293. https://doi.org/10.1016/0016-7037(88)90084-1

Kushiro, I. (1976). Changes in viscosity and structure of melt of $NaAlSi_2O_6$ composition at high pressures. *Journal of Geophysical Research*, *81*(35), 6347–6350. https://doi.org/10.1029/jb081i035p06347

Kushiro, I. (1978). Viscosity and structural changes of albite ($NaAlSi_3O_8$) melt at high pressures. *Earth and Planetary Science Letters*, *41*(1), 87–90. https://doi.org/10.1016/0012-821x(78)90044-4

Kushiro, I., Yoder, H. S., & Mysen, B. O. (1976). Viscosities of basalt and andesite melts at high pressures. *Journal of Geophysical Research*, *81*(35), 6351–6356. https://doi.org/10.1029/jb081i035p06351

Ladenburg, R. (1907). Über den Einfluß von Wänden auf die Bewegung einer Kugel in einer reibenden Flüssigkeit. *Annalen der Physik*, *328*(8), 447–458. https://doi.org/10.1002/andp.1907328080

Lange, R. A. (1997). A revised model for the density and thermal expansivity of K_2O-Na_2O-CaO-MgO-Al_2O_3-SiO_2 liquids from 700 to 1900 K: Extension to crustal magmatic temperatures. *Contributions to Mineralogy and Petrology*, *130*, 1–11. https://doi.org/10.1007/s004100050345

Lange, R. A., & Carmichael, I. S. E. (1987). Densities of Na_2O-K_2O-CaO-MgO-FeO-Fe_2O_3-Al_2O_3-TiO_2-SiO_2 liquids: New measurements and derived partial molar properties. *Geochimica et Cosmochimica*, *51*(11), 2931–2946. https://doi.org/10.1016/0016-7037(87)90368-1

Laumonier, M., Scaillet, B., Pichavant, M., Champallier, R., Andujar, J., & Arbaret, L. (2014). On the conditions of magma mixing and its bearing on andesite production in the crust. *Nature Communications*, *5*(1), 5607. https://doi.org/10.1038/ncomms6607

LeBlanc, G. E., & Secco, R. A. (1995). High pressure Stokes' viscometry: A new in situ technique for sphere velocity determination. *Review of Scientific Instruments*, *66*(10), 5015–5018. https://doi.org/10.1063/1.1146125

LeBlanc, G. E., & Secco, R. A. (1996). Viscosity of an Fe-S liquid up to 1300°C and 5 GPa. *Geophysical Research Letters*, *23*(3), 213–216. https://doi.org/10.1029/96gl00216

Leinenweber, K. D., Tyburczy, J. A., Sharp, T. G., Soignard, E., Diedrich, T., Petuskey, W. B., et al. (2012). Cell assemblies for reproducible multi-anvil experiments (the COMPRES assemblies). *American Mineralogist*, *97*(2–3), 353–368. https://doi.org/10.2138/am.2012.3844

Liebske, C., Schmickler, B., Terasaki, H., Poe, B. T., Suzuki, A., Funakoshi, K. I., et al. (2005). Viscosity of peridotite liquid up to 13 GPa: Implications for magma ocean viscosities. *Earth and Planetary Science Letters*, *240*(3–4), 589–604. https://doi.org/10.1016/j.epsl.2005.10.004

Lorentz, H. A. (1907). Ein allgemeiner Satz, die Bewegung einer reibenden Flüssigkeit betreffend, nebst einigen Anwendungen desselben. *Abhandlungen über Theoretische Physik*, *1*, 23.

Manning, C. (2004). The chemistry of subduction-zone fluids. *Earth and Planetary Science Letters*, *223*(1–2), 1–16. https://doi.org/10.1016/j.epsl.2004.04.030

Maude, A. D. (1961). End effects in a falling-sphere viscometer. *Journal of Applied Physics*, *12*(6), 293–295. https://doi.org/10.1088/0508-3443/12/6/306

Mibe, K., Chou, I. M., & Bassett, W. A. (2008). In situ Raman spectroscopic investigation of the structure of subduction-zone fluids. *Journal of Geophysical Research*, *113*(B4), B04208. https://doi.org/10.1029/2007jb005179

Mitra, N. R., Decker, D. L., & Vanfleet, H. B. (1967). Melting curves of copper, silver, gold, and platinum to 70 kbar. *Physical Review*, *161*(3), 613–617. https://doi.org/10.1103/physrev.161.613

Mori, S., Ohtani, E., & Suzuki, A. (2000). Viscosity of the albite melt to 7 GPa at 2000 K. *Earth and Planetary Science Letters*, *175*(1–2), 87–92. https://doi.org/10.1016/s0012-821x(99)00284-8

Mouser, M. D., Dygert, N., Anzures, B. A., Grambling, N. L., Hrubiak, R., Kono, Y., et al. (2021). Experimental investigation of Mercury's magma ocean viscosity: Implications for the formation of Mercury's cumulate mantle, its subsequent dynamic evolution, and crustal petrogenesis. *Journal of Geophysical Research: Planets*, *126*(11), e2021JE006946. https://doi.org/10.1029/2021JE006946

Naif, S., Key, K., Constable, S., & Evans, R. L. (2013). Melt-rich channel observed at the lithosphere–asthenosphere boundary. *Nature*, *495*(7441), 356–359. https://doi.org/10.1038/nature11939

Neilson, R. T., Spera, F. J., & Ghiorso, M. S. (2016). Thermodynamics, self-diffusion, and structure of liquid $NaAlSi_3O_8$ to 30 GPa by classical molecular dynamics simulations. *American Mineralogist*, *101*(9), 2029–2040. https://doi.org/10.2138/am-2016-5486

Ochs, F. A., & Lange, R. A. (1997). The partial molar volume, thermal expansivity and compressibility of H_2O in $NaAlSi_3O_8$ liquid: New measurements and an internally consistent model. *Contributions to Mineralogy and Petrology*, *129*(2–3), 155–165. https://doi.org/10.1007/s004100050329

Ono, S. (2022). Equation of state determination for rhenium using first-principles molecular dynamics calculations and high-pressure experiments. *Advances in Condensed Matter Physics*, *2022*, 1–6. https://doi.org/10.1155/2022/7545777

Pierru, R., Andrault, D., Manthilake, G., Monteux, J., Luc Devidal, J., Guignot, N., et al. (2022). Deep mantle origin of large igneous provinces and komatiites. *Science Advances*, *8*(44), eabo1036. https://doi.org/10.1126/sciadv.abo1036

Poe, B. T., McMillan, P. F., Rubie, D. C., Chakraborty, S., Yarger, J., & Diefenbacher, J. (1997). Silicon and oxygen self-diffusivities in silicate liquids measured to 15 gigapascals and 2800 Kelvin. *Science*, *276*(5316), 1245–1248. https://doi.org/10.1126/science.276.5316.1245

Poe, B. T., Romano, C., Liebske, C., Rubie, D. C., Terasaki, H., Suzuki, A., & Funakoshi, K. (2006). High-temperature viscosity measurements of hydrous albite liquid using in-situ falling-sphere viscometry at 2.5 GPa. *Chemical Geology*, *229*(1–3), 2–9. https://doi.org/10.1016/j.chemgeo.2006.01.010

Rai, N., Perrillat, J. P., Mezouar, M., Colin, A., Petitgirard, S., & van Westrenen, W. (2019). In situ viscometry of primitive lunar magmas at high pressure and high temperature. *Frontiers in Earth Science*, *7*. https://doi.org/10.3389/feart.2019.00094

Reid, J. E., Suzuki, A., Funakoshi, K., Terasaki, H., Poe, B. T., Rubie, D. C., & Ohtani, E. (2003). The viscosity of $CaMgSi_2O_6$ liquid at pressures up to 13 GPa. *Physics of the Earth and Planetary Interiors*, *139*(1–2), 45–54. https://doi.org/10.1016/s0031-9201(03)00143-2

Revenaugh, J., & Sipkin, S. A. (1994). Seismic evidence for silicate melt atop the 410-km mantle discontinuity. *Nature*, *369*(6480), 474–476. https://doi.org/10.1038/369474a0

Ross, A. R., Thybo, H., & Solidilov, L. N. (2004). Reflection seismic profiles of the core-mantle boundary. *Journal of Geophysical Research*, *109*(B8), B08303. https://doi.org/10.1029/2003jb002515

Rost, S., Garnero, E. J., Williams, Q., & Manga, M. (2005). Seismological constraints on a possible plume root at the core–mantle boundary. *Nature*, *435*(7042), 666–669. https://doi.org/10.1038/nature03620

Rubie, D. C., Ross, C. R., Carroll, M. R., & Elphick, S. C. (1993). Oxygen self-diffusion in $Na_2Si_4O_9$ liquid up to 10 GPa and estimation of high-pressure melt viscosities. *American Mineralogist*, *78*, 574–582.

Rutter, M. D., Secco, R. A., Liu, H., Uchida, T., Rivers, M. L., Sutton, S. R., & Wang, Y. (2002). Viscosity of liquid Fe at high pressure. *Physical Review B: Condensed Matter and Materials Physics*, *66*(6), 601021–601024. https://doi.org/10.1103/physrevb.66.060102

Rutter, M. D., Secco, R. A., Uchida, T., Liu, H., Wang, Y., Rivers, M. L., & Sutton, S. R. (2002). Towards evaluating the viscosity of the Earth's outer core: An experimental high pressure study of liquid Fe-S (8.5 wt.% S). *Geophysical Research Letters*, *29*(8), 58-1–58-4. https://doi.org/10.1029/2001GL014392

Sakamaki, T., Suzuki, A., Ohtani, E., Terasaki, H., Urakawa, S., Katayama, Y., et al. (2013). Ponded melt at the boundary between the lithosphere and asthenosphere. *Nature Geoscience*, *6*(12), 1041–1044. https://doi.org/10.1038/ngeo1982

Schaefer, L., & Elkins-Tanton, L. T. (2016). Magma oceans as a critical stage in the tectonic development of rocky planets. *Philosophical Transactions of the Royal Society A: Mathematical*, *376*(2132), 113–139. https://doi.org/10.1098/rsta.2018.0109

Schmandt, B., Jacobsen, S. D., Becker, T. W., Liu, Z., & Dueker, K. G. (2014). Dehydration melting at the top of the lower mantle. *Science*, *344*(6189), 1256–1268. https://doi.org/10.1126/science.1253358

Schulze, F., Behrens, H., Holtz, F., Roux, J., & Johannes, W. (1996). The influence of H_2O on the viscosity of a haplogranitic melt. *American Mineralogist*, *81*(9–10), 1155–1165. https://doi.org/10.2138/am-1996-9-1014

Secco, R. A. (1994). High pressure measurements of viscosities of Fe-S liquids. *AIP Conference Proceedings*, *309*, 947–949. https://doi.org/10.1063/1.46191

Secco, R. A., Rutter, M. D., Balog, S. P., Liu, H., Rubie, D. C., Uchida, T., et al. (2002). Viscosity and density of Fe–S liquids at high pressures. *Journal of Physics: Condensed Matter*, *14*(44), 11325–11330. https://doi.org/10.1088/0953-8984/14/44/476

Shaw, H. R. (1963). Obsidian-H_2O viscosities at 1000 and 2000 bars in the temperature range 700° to 900°C. *Journal of Geophysical Research*, *68*(23), 6337–6343. https://doi.org/10.1029/jz068i023p06337

Shen, A. H., & Keppler, H. (1997). Direct observation of complete miscibility in the albite-H_2O system. *Nature*, *385*(6618), 710–712. https://doi.org/10.1038/385710a0

Shimada, M. (1972). Melting of albite at high pressures under conditions. *Journal of Physical Earth*, *20*(1), 59–70. https://doi.org/10.4294/jpe1952.20.59

Spice, H., Sanloup, C., Cochain, B., de Grouchy, C., & Kono, Y. (2015). Viscosity of liquid fayalite up to 9 GPa. *Geochimica et Cosmochimica*, *148*, 219–227. https://doi.org/10.1016/j.gca.2014.09.022

Stagno, V., Kono, Y., Stopponi, V., Masotta, M., Scarlato, P., & Manning, C. E. (2020). The viscosity of carbonate-silicate transitional melts at Earth's upper mantle pressures and temperatures, determined by the in situ falling-sphere technique. *Carbon in Earth's Interior*, 223–236.

Stagno, V., Stopponi, V., Kono, Y., D'Arco, A., Lupi, S., Romano, C., et al. (2020). The viscosity and atomic structure of volatile-bearing melilititic melts at high pressure and temperature and the transport of deep carbon. *Minerals*, *10*(3), 267. https://doi.org/10.3390/min10030267

Stagno, V., Stopponi, V., Kono, Y., Manning, C. E., & Irifune, T. (2018). Experimental determination of the viscosity of Na_2CO_3 melt between 1.7 and 4.6 GPa at 1200–1700°C: Implications for the rheology of carbonatite magmas in the Earth's upper mantle. *Chemical Geology*, *501*, 19–25. https://doi.org/10.1016/j.chemgeo.2018.09.036

Stimson, M., & Jeffery, G. B. (1926). The motion of two spheres in a viscous fluid. *Proceedings of the Royal Society of London. Series A, Containing Papers of a Mathematical and Physical Character*, *111*, 110–116.

Stolper, E., Walker, D., Hager, B. H., & Hays, J. F. (1981). Melt segregation from partially molten source regions: The importance of melt density and source region size. *Journal of Geophysical Research*, *86*(B7), 6261–6271. https://doi.org/10.1029/jb086ib07p06261

Sutterby, J. L. (1973). Falling sphere viscometry - 1. Wall and inertial corrections to Stokes' Law in long tubes. *Transactions of the Society of Rheology*, *17*(4), 559–573. https://doi.org/10.1122/1.549308

Suzuki, A. (2018). Effect of carbon dioxide on the viscosity of a melt of jadeite composition at high pressure. *Journal of Mineralogical and Petrological Sciences*, *113*(1), 47–50. https://doi.org/10.2465/jmps.170717

Suzuki, A. (2019a). Viscosity of $K_2TiSi_4O_{11}$ melt at high pressure. *Journal of Mineralogical and Petrological Sciences*, *114*(6), 280–283. https://doi.org/10.2465/jmps.190730

Suzuki, A. (2019b). Viscosity of melt of soda melilite composition at high pressure. *Journal of Mineralogical and Petrological Sciences*, *114*(1), 41–44. https://doi.org/10.2465/jmps.180710

Suzuki, A., Ohtani, E., Funakoshi, K., Terasaki, H., & Kubo, T. (2002). Viscosity of albite melt at high pressure and high temperature. *Physics and Chemistry of Minerals*, *29*(3), 159–165. https://doi.org/10.1007/s00269-001-0216-4

Suzuki, A., Ohtani, E., Terasaki, H., & Funakoshi, K. (2005). Viscosity of silicate melts in $CaMgSi_2O_6$-$NaAlSi_2O_6$ system at high pressure. *Physics and Chemistry of Minerals*, *32*(2), 140–145. https://doi.org/10.1007/s00269-005-0452-0

Suzuki, A., Ohtani, E., Terasaki, H., Nishida, K., Hayashi, H., Sakamaki, T., et al. (2011). Pressure and temperature dependence of the viscosity of a $NaAlSi_2O_6$ melt. *Physics and Chemistry of Minerals*, *38*(1), 59–64. https://doi.org/10.1007/s00269-010-0381-4

Syracuse, E. M., van Keken, P. E., & Abers, G. A. (2010). The global range of subduction zone thermal models. *Physics of the Earth and Planetary Interiors*, *183*(1–2), 73–90. https://doi.org/10.1016/j.pepi.2010.02.004

Tange, Y., Nishihara, Y., & Tsuchiya, T. (2009). Unified analyses for *P-V-T* equation of state of MgO: A solution for pressure-scale problems in high *P-T* experiments. *Journal of Geophysical Research*, *114*(B3), 1–16. https://doi.org/10.1029/2008jb005813

Tanner, R. I. (1963). End effects in falling-ball viscometry. *Journal of Fluid Mechanics*, *17*(2), 161–170. https://doi.org/10.1017/s002211206300121x

Tauzin, B., Debayle, E., & Wittlinger, G. (2010). Seismic evidence for a global low-velocity layer within the Earth's upper mantle. *Nature Geoscience*, *3*(10), 718–721. https://doi.org/10.1038/ngeo969

Tenner, T. J., Lange, R. A., & Downs, R. T. (2007). The albite fusion curve re-examined: New experiments and the high-pressure density and compressibility of high albite and $NaAlSi_3O_8$ liquid. *American Mineralogist*, *92*(10), 1573–1585. https://doi.org/10.2138/am.2007.2464

Terasaki, H., Kato, T., Funakoshi, K., Suzuki, A., & Urakawa, S. (2004). Viscosity of liquid sulfur under high pressure. *Journal of Physics: Condensed Matter*, *16*(10), 1707–1714. https://doi.org/10.1088/0953-8984/16/10/003

Terasaki, H., Kato, T., Urakawa, S., Funakoshi, K., Sato, K., Suzuki, A., & Okada, T. (2002). Viscosity change and structural transition of Molten Fe at 5 GPa. *Geophysical Research Letters*, *29*(8). 68-1–68-3. https://doi.org/10.1029/2001GL014321

Terasaki, H., Kato, T., Urakawa, S., Funakoshi, K. I., Suzuki, A., Okada, T., et al. (2001). The effect of temperature, pressure, and sulfur content on viscosity of the Fe–FeS melt. *Earth and Planetary Science Letters*, *190*(1–2), 93–101. https://doi.org/10.1016/s0012-821x(01)00374-0

Terasaki, H., Suzuki, A., Ohtani, E., Nishida, K., Sakamaki, T., & Funakoshi, K. (2006). Effect of pressure on the viscosity of Fe-S and Fe-C liquids up to 16 GPa. *Geophysical Research Letters*, *33*(22), L22307. https://doi.org/10.1029/2006GL027147

Tinker, D., Lesher, C. E., Baxter, G. M., Uchida, T., & Wang, Y. (2004). High-pressure viscometry of polymerized silicate melts and limitations of the Eyring equation. *American Mineralogist*, *89*(11–12), 1701–1708. https://doi.org/10.2138/am-2004-11-1216

Urakawa, S., Terasaki, H., Funakoshi, K., Kato, T., & Suzuki, A. (2001). Radiographic study on the viscosity of the Fe-FeS melts at the pressure of 5 to 7 GPa. *American Mineralogist*, *86*(4), 578–582. https://doi.org/10.2138/am-2001-0420

Vetere, F., Behrens, H., Holtz, F., & Neuville, D. R. (2006). Viscosity of andesitic melts-new experimental data and a revised calculation model. *Chemical Geology*, *228*(4), 233–245. https://doi.org/10.1016/j.chemgeo.2005.10.009

Vetere, F., Behrens, H., Schuessler, J. A., Holtz, F., Misiti, V., & Borchers, L. (2008). Viscosity of andesite melts and its implication for magma mixing prior to Unzen 1991–1995 eruption. *Journal of Volcanology and Geothermal Research*, *175*(1–2), 208–217. https://doi.org/10.1016/j.jvolgeores.2008.03.028

Vidale, J. E., & Hedlin, M. A. (1998). Evidence for partial melt at the core–mantle boundary north of Tonga from the strong scattering of seismic waves. *Nature*, *391*(6668), 682–685. https://doi.org/10.1038/35601

Wang, Y., Rivers, M., Sutton, S., Nishiyama, N., Uchida, T., & Sanehira, T. (2009). The large-volume high-pressure facility at GSECARS: A "Swiss-army-knife" approach to synchrotron-based experimental studies. *Physics of the Earth and Planetary Interiors*, *174*(1–4), 270–281. https://doi.org/10.1016/j.pepi.2008.06.017

White, B., & Montana, A. (1990). The effect of H_2O and CO_2 on the viscosity of sanidine liquid at high pressures. *Journal of Geophysical Research*, *95*(B10), 15683–15693. https://doi.org/10.1029/jb095ib10p15683

Whittington, A. G., Hellwig, B. M., Behrens, H., Joachim, B., Stechern, A., & Vetere, F. (2009). The viscosity of hydrous dacitic liquids: Implications for the rheology of evolving silicic magmas. *Bulletin of Volcanology*, *71*(2), 185–199. https://doi.org/10.1007/s00445-008-0217-y

Xie, L., Yamazaki, D., Manthilake, G., Higo, Y., Tange, Y., Guignot, N., et al. (2020). Formation of bridgmanite-enriched layer at the top lower-mantle during magma ocean solidification. *Nature Communications*, *11*, 1–10.

Xie, L., Yoneda, A., Katsura, T., Andrault, D., Tange, Y., & Higo, Y. (2021). Direct viscosity measurement of peridotite melt to lower-mantle conditions: A further support for a fractional magma-ocean solidification at the top of the lower mantle. *Geophysical Research Letters*, *48*(19), 1–8. https://doi.org/10.1029/2021gl094507

Yang, L., Karandikar, A., & Boehler, R. (2012). Flash heating in the diamond cell: Melting curve of rhenium. *Review of Scientific Instruments*, *83*(6), 2–7. https://doi.org/10.1063/1.4730595

Zeff, G., & Williams, Q. (2019). Fractional crystallization of martian magma oceans and formation of a thermochemical boundary layer at the base of the mantle. *Geophysical Research Letters*, *46*(20), 10997–11007. https://doi.org/10.1029/2019gl084810

Zha, C. S., Mibe, K., Bassett, W. A., Tschauner, O., Mao, H. K., & Hemley, R. J. (2008). P-V-T equation of state of platinum to 80 GPa and 1900 K from internal resistive heating/X-ray diffraction measurements. *Journal of Applied Physics*, *103*(5), 054908. https://doi.org/10.1063/1.2844358

Zhang, G. H., & Chou, K. C. (2012). Correlation between viscosity and electrical conductivity of aluminosilicate melts. *Metallurgical and Materials Transactions B: Process Metallurgy and Materials Processing Science*, *43*(4), 849–855. https://doi.org/10.1007/s11663-012-9674-y

Zhu, F., Lai, X., Wang, J., Williams, Q., Liu, J., Kono, Y., & Chen, B. (2022). Viscosity of Fe-Ni-C liquids up to core pressures and implications for dynamics of planetary cores. *Geophysical Research Letters*, *49*(4), e2021GL095991. https://doi.org/10.1029/2021gl095991